



# Hydrography and circulation below Fimbulisen Ice Shelf, East Antarctica, from 12 years of moored observations

Julius Lauber<sup>1,2</sup>, Tore Hattermann<sup>1</sup>, Laura de Steur<sup>1</sup>, Elin Darelius<sup>2,3</sup>, and Agneta Fransson<sup>1</sup>

<sup>1</sup>Norwegian Polar Institute, Tromsø, Norway

<sup>2</sup>Geophysical Institute, University of Bergen, Bergen, Norway

<sup>3</sup>Bjerknes Centre for Climate Research, Bergen, Norway

**Correspondence:** Julius Lauber (julius.lauber@outlook.com)

**Abstract.** Future mass loss from the East Antarctic Ice Sheet represents a major uncertainty in projections of future sea level rise. Recent studies have highlighted the potential vulnerability of the East Antarctic Ice Sheet to atmospheric and oceanic changes, but long-term observations inside the ice shelf cavities are rare, especially in East Antarctica. Here, we present new insights from observations from three oceanic moorings below Fimbulisen Ice Shelf from 2009 to 2021. We examine the characteristics of Warm Deep Water (WDW) intrusions across a sill connecting the cavity to the open ocean, and investigate seasonal variability of the circulation and water masses inside the cavity. In autumn, solar-heated, buoyant Antarctic Surface Water (ASW) reaches below the 350 m deep central part of the ice shelf, separating colder Ice Shelf Water from the ice base and affecting the cavity circulation on seasonal timescales. At depth, the occurrence of WDW is associated with the advection of cyclonic eddies across the sill into the cavity. These eddies reach up to the ice base. The warm intrusions occur favorably from January to March and from September to November, and traces of WDW-derived meltwater close to the ice base imply an overturning of these warm intrusions inside the cavity. We suggest that both the offshore thermocline depth and interactions of the Antarctic Slope Current with the ice shelf topography over the continental slope cause this timing. Our findings provide a better understanding of the interplay between shallow ASW and deep WDW inflows for basal melting at Fimbulisen, with implications for the potential vulnerability of the ice shelf to climate change.

## 1 Introduction

Mass loss from the Antarctic ice sheet is certain to contribute to future sea level rise (DeConto and Pollard, 2016; DeConto et al., 2021). Ice shelf thinning through basal melting (Pritchard et al., 2012) and iceberg calving (Greene et al., 2022) is the main source for this mass loss, as it reduces the buttressing of the inland ice and can accelerate its discharge (Dupont and Alley, 2005; Reese et al., 2018). Still, major uncertainties in future sea level rise projections originate from the Antarctic ice sheet (Edwards et al., 2021). The West Antarctic ice shelves are subject to rapid basal mass loss of up to tens of  $\text{m year}^{-1}$  (Rignot et al., 2013; Adusumilli et al., 2020), which has been attributed to direct access of Circumpolar Deep Water (CDW) to the cavities (e.g., Dutrieux et al., 2014; Jenkins et al., 2018). In contrast, most East Antarctic ice shelves experience lower basal melt rates in the order of  $1 \text{ m year}^{-1}$  (Adusumilli et al., 2020). However, in recent years, observations have revealed that some East Antarctic ice shelves are more exposed to warm water masses and subject to associated basal melting than previously



25 thought (Rintoul et al., 2016; Hirano et al., 2020; Lauber et al., 2023c; Ribeiro et al., 2023). These localized observations coincide with a long-term warming and poleward shift of CDW off East Antarctica, with possible implications of increased basal melting of this part of the ice sheet (Herraiz-Borreguero and Naveira Garabato, 2022). Yet, most East Antarctic ice shelf cavities remain unexplored to date, so the governing oceanic processes and the response of the ice shelves to oceanic changes remain uncertain.

30 Fimbulisen Ice Shelf is located at the prime meridian at the coast of the southern Weddell Gyre and is the seaward extension of the Jutulstraumen ice stream. The northernmost portion of the ice shelf, Trolltunga, overhangs the continental shelf break by several tens of kilometers (Fig. 1a, Nøst, 2004). In this region and along the whole Dronning Maud Land coast, Warm Deep Water (WDW), a derivative of CDW that has been advected poleward within the eastern limb of the Weddell Gyre, is located in the direct vicinity of the ice shelves off the narrow continental shelf. In front of the ice shelves, the WDW is suppressed due  
35 to prevailing easterly winds which induce a southward Ekman transport and downwelling at the coast (Sverdrup, 1954). This creates the Antarctic Slope Front (ASF) and the associated westward geostrophic Antarctic Slope Current (ASC, Jacobs, 1991; Thompson et al., 2018), to which Trolltunga is directly exposed. The ASF shields the cavities from most of the WDW and thus prevents high basal melt rates, although small amounts of WDW have been observed to access the continental shelf through eddies as part of the ASF overturning (Nøst et al., 2011).

40 Most of the water inside the Fimbulisen cavity is close to the surface freezing temperature (Nicholls et al., 2006, 2008). This water mass originates from surface cooling and the addition of salt during the sea ice freezing season in the open ocean and is referred to as Winter Water (WW, Nicholls et al., 2009). In turn, surface warming and sea ice melt around summer add heat and freshwater to the coastal water column, creating a lighter water mass called Antarctic Surface Water (ASW, Nicholls et al.,  
45 2014; Hattermann et al., 2012). When any of the three coastal water masses (ASW, WW, WDW) comes in direct contact with the ice shelf, the ice will melt at a rate depending on the thermal forcing (Jenkins, 1999), i.e. the difference between the ocean temperature and the in-situ freezing point. Turbulence in the ice-ocean boundary layer below the ice controls the efficiency of the heat transfer toward the ice base (McPhee and Morison, 2001). Basal melting produces glacial meltwater (GMW, Jenkins, 1999), and if the mixing product with the adjacent cavity water masses is colder than the surface freezing temperature, the  
50 water is called Ice Shelf Water (ISW, Foldvik et al., 2004). Due to the GMW input, ISW is less saline and hence more buoyant than its oceanic source, such that it typically rises along the ice shelf base (Nøst and Foldvik, 1994). The mixing of a water mass with GMW occurs along a straight line in temperature-salinity space (Gade, 1979). These mixing lines have been used to infer overturning inside the Fimbulisen cavity by relating water masses observed close to the seafloor and below the ice base (Nicholls et al., 2008; Hattermann et al., 2012).

55 Several modeling studies have investigated the oceanic conditions below Fimbulisen. In particular, Smedsrud et al. (2006) suggested the deep ASC to modulate the inflow of WDW into the cavity via bottom Ekman transport. This mechanism was supported by observations of the ASC in front of Trolltunga (Núñez-Riboni and Fahrbach, 2009). Hattermann et al. (2014) found that during summer, the circulation below Fimbulisen at the seafloor follows the bathymetry and the circulation below the ice base follows the ice shelf draft. These baroclinic conditions were attributed to increased stratification during that season.



60 In turn, in winter, Hattermann et al. (2014) found more barotropic conditions due to a well-mixed water column that allows for less vertical shear. Furthermore, Hattermann et al. (2014) found a distinct seasonal cycle in WDW inflow, related to an amplitude of  $0.4^{\circ}\text{C}$  of the temperature seasonal cycle at the inflow path, but not favored by a shallow offshore WDW layer. These modeling results, however, have only been validated by direct observations to a very limited extent.

Hattermann et al. (2012) and Lauber et al. (2023c) have discussed the variability of WDW inflows on interannual timescales. 65 Lauber et al. (2023c) argued that these warm inflows occurred more frequently when the offshore WDW (and the associated thermocline) shoaled and shifted southward, driven by changes in local and remote winds and sea ice cover, although the detailed dynamics of the warm inflows were not further investigated. The thermocline depth over the 1100 m isobath 450 km upstream of Fimbulisen was observed to be the shallowest in March based on mooring observations from 2019 to 2020 (Lauber et al., 2023a). However, there was no evident increase in sub-ice-shelf temperatures during this period. Lauber et al. (2023a) 70 therefore suggested that additional processes like bottom Ekman transport (Smedsrud et al., 2006; Núñez-Riboni and Fahrbach, 2009) and potential vorticity dynamics at the ice front (Wählin et al., 2020; Steiger et al., 2022) may locally modulate the WDW access to the cavity.

A regime shift toward more sustained WDW inflow below Fimbulisen was observed in 2016, associated with an almost doubling of the long-term basal melt rate of  $0.67\text{ m year}^{-1}$  (Lauber et al., 2023c). To improve projections of future changes, 75 a more detailed understanding of the oceanic processes below the ice shelf is needed. To address this issue, we analyze 12 years (2009-2021) of near-continuous oceanographic observations of temperature, dissolved oxygen, velocity, and (to a limited extent) salinity from six instruments on three moorings below Fimbulisen. Based on these data, we investigate the hourly to seasonal variability of the hydrography and circulation inside the cavity. We characterize the WDW intrusions at depth and perform an Optimum Multiparameter analysis to quantify the water mass composition inside the cavity. The sub-ice-shelf 80 moorings, auxiliary data of open-ocean hydrography, and methods are described in Sect. 2. The mooring time series, derived water mass distributions, and details of WDW intrusions are presented in Sect. 3. Implications of the results are discussed in Sect. 4 and conclusions are summarized in Sect. 5.

## 2 Data and Methods

### 2.1 Sub-ice-shelf moorings

85 Three oceanographic moorings (M1-3) were deployed through hot-water-drilled boreholes below Fimbulisen Ice Shelf in December 2009 and January 2010 (Fig. 1, Hattermann et al., 2012). M1 was placed over the deepest connection between the open ocean and the cavity. This connection is a sill of 570 m depth that crosscuts the continental slope (referred to as main sill hereafter, Nøst, 2004) and is the most reasonable pathway for WDW to enter the cavity. M2 was located 50 km southeast of M1 following contours of water column thickness into the cavity, as WDW intruding the cavity at the main sill is expected to follow 90 these contours (Hattermann et al., 2012). M3 was located below the eastern part of the ice shelf downstream of a shallower sill of 420 m depth, where a secondary WDW inflow pathway has been proposed (Nicholls et al., 2006). The moorings were equipped with two instruments each, an upper one around 30 m below the ice base, and a lower one around 100 m above the



seafloor. In the following, these instruments are referred to as  $M1_{\text{lower}}$ ,  $M2_{\text{upper}}$ , etc. Centered at the prime meridian, the keel of Jutulstraumen dominates the ice thickness of Fimbulisen. Here, the ice shelf draft is more than 300 m deep, compared to 100-200 m west and east of the keel (Fig. 1b).  $M1$  was located on the western side of the keel, and  $M2$  was located right below it in a southwest-northeast oriented 1.5 km wide and 75 m deep basal channel.  $M3$  was east of the Jutulstraumen keel. The depths of the instruments, the ice draft and water depth at the moorings, and their horizontal displacement due to ice velocity are given in Table 1. All six instruments were Aandera RCM9 equipped with an Optode 3830, and measured temperature, conductivity, dissolved oxygen, and horizontal velocity at hourly intervals. All sensors were calibrated before deployment. The data until January 2012 have been analyzed in Hattermann et al. (2012), and the data until January 2019 in Lauber et al. (2023c). The latest data were recovered in February 2022, with data recorded until December 2021 when the batteries ran out. Gaps in some variables were caused by temporary or permanent instrument failures. Spikes outside the reasonable ranges of the variables were removed after visual inspection.

The temperature sensors delivered stable temperature records over 12 years. For comparison between water masses, conservative temperature was calculated following TEOS-10 and the Gibbs-SeaWater Toolbox (McDougall and Barker, 2011).

The conductivity sensors drifted at all instruments, at the latest from the end of 2010 on. At  $M3_{\text{upper}}$ , no conductivity was recorded at all. At all other instruments, the conductivity data collected after December 2010 were discarded. At  $M1_{\text{upper}}$ , the drift-corrected data provided by Hattermann et al. (2012) until November 2010 were used. Using the Gibbs-SeaWater Toolbox (McDougall and Barker, 2011), conductivity was converted into absolute salinity.

The dissolved oxygen data did not show any obvious sensor drift, but the values at all six instruments were systematically  $0.4 \text{ ml l}^{-1}$  larger than in comparable data sets (Sect. 2.2). In addition, the oxygen records contained noise in the form of spikes to low values, mainly at the lowest measured temperatures. Detailed steps to remove the offset and the noise are described in Appendix A. Discarding bad data during the correction process introduced data gaps of up to several months toward the end of the record at  $M2_{\text{upper}}$  and  $M3_{\text{upper}}$ .

The measured velocities were corrected for magnetic declination using magnetic field data from the International Geomagnetic Reference Field (Alken et al., 2021) on hourly resolution.

We used the following toolboxes for data analysis and visualization: jLab (Lilly, 2021),  $M\_Map$  (Pawlowicz, 2023), cmocean (Thyng et al., 2016), and Antarctic Mapping Tools (Greene et al., 2017).

## 2.2 Auxiliary data sets

For comparison to the sub-ice-shelf mooring observations, we used open ocean temperature, salinity, and dissolved oxygen data collected in front of Fimbulisen (Fig. 1a): we used CTD data from 14 stations taken during the Troll Transect cruise onboard *M/V Malik Arctica* in December 2020 and January 2021 using an SBE911plus (Lauber et al., 2023a). Additionally, we used hourly mooring data from three Sea-Bird SBE37 MicroCATS at two locations on the continental slope from March 2019 to December 2020. Of these three MicroCATS, one was mounted on  $DML_{\text{deep}}$  at a depth of 130 m, and two were mounted on  $DML_{\text{shallow}}$  at depths of 210 m and 390 m (Lauber et al., 2023a). On top, we used dissolved oxygen data obtained from Winkler titration from 136 water samples at 17 stations taken during the Southern Ocean Ecosystem cruise onboard *R/V*

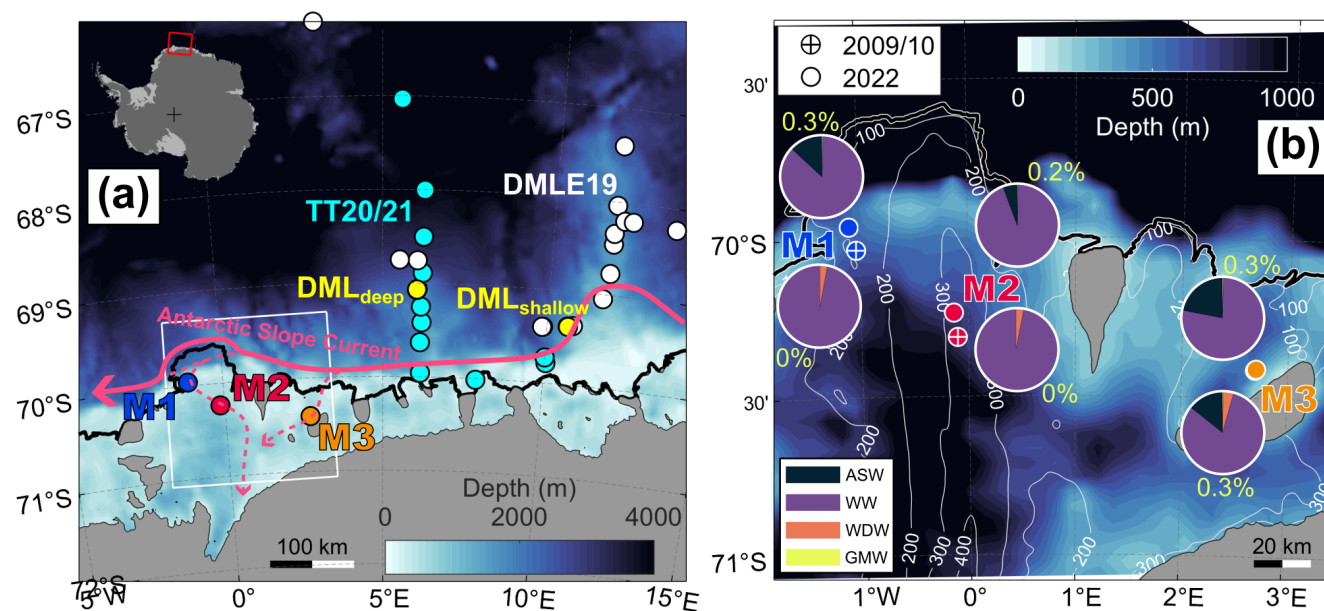


**Figure 1.** (a) Map of the study area indicating the positions of the sub-ice-shelf moorings M1-3 in 2022 (blue, red, and orange dots), offshore moorings DML<sub>deep</sub> and DML<sub>shallow</sub> (yellow dots), Troll Transect 2020/21 (TT20/21) CTD stations (cyan dots), and Southern Ocean Ecosystem cruise 2019 (DMLE19) CTD stations (white dots). The magenta arrow indicates the Antarctic Slope Current and possible pathways of Warm Deep Water into the cavity and toward the grounding line. The white box marks the zoomed area in panel (b). The colormap shows the bathymetry from Eisermann et al. (2020a) south of 69°S, from Eisermann et al. (2024) east of 8°E, and from Dorschel et al. (2022, IBCSO v2) otherwise. The black line indicates the ice front and coastline (Mouginot et al., 2017), and gray patches are grounded ice (Mouginot et al., 2017). (b) Zoomed area showing the M1-3 positions in 2009 and 2022. Pie charts indicate the estimated mean water mass distribution in 2010 estimated from the Optimum Multiparameter analysis for all upper (indicated north of the location) and lower (indicated south of the location) instruments. Yellow numbers show the GMW concentration, which is not visible in the pie charts. The colormap shows the bathymetry from Eisermann et al. (2020a), and white contours indicate the 10 km-smoothed ice shelf draft in meters (Morlighem et al., 2020).

*Kronprins Haakon* in March 2019. The respective temperature and salinity values were taken from Sea-Bird SBE911plus CTD measurements. The Winkler titration provides the most reliable measurements of dissolved oxygen. The MicroCAT and CTD oxygen sensors were calibrated before and after deployment, but can be subject to temporal sensor drift.

130 In addition, we used temperature and salinity records obtained from a glider operating between December 2020 to April 2021 from 0° to 7°E and from 69.5°S to 66.5°S.

Monthly values of thermocline depth, defined as the depth of the  $-0.3^{\circ}\text{C}$  isotherm, were extracted from hydrographic climatology at 17°W (Hattermann, 2018) and from the DML<sub>shallow</sub> mooring records (Lauber et al., 2023a).



**Table 1.** Ice shelf draft and water depth at deployment in 2009/10, median instrument depths and horizontal displacement of all mooring instruments.

	M1	M2	M3
Ice shelf draft (2009/10)	185 m	350 m	158 m
Upper instrument depth	223 m	368 m	197 m
Lower instrument depth	542 m	681 m	451 m
Water depth (2009/10)	653 m	870 m	535 m
Horizontal displacement (2009/10-2022)	8.50 km	8.64 km	0.52 km

### 2.3 Water mass analysis

135 We investigated the water mass composition at all instruments using Optimum Multiparameter analysis (OMP, described in, e.g., Tomczak, 1981; Tomczak and Large, 1989; Mackas et al., 1987). With this method, the concentrations of given source water masses within an observed water mass can be obtained by solving a linear system of equations, assuming the conservation of specified tracers. In our case, the source water masses were ASW, WW, WDW, and GMW, and the tracers were conservative temperature, absolute salinity, and dissolved oxygen. The latter can be regarded as a conservative tracer below an ice shelf, assuming that biological productivity and respiration which would modify oxygen levels are negligible (Jenkins, 1999). The equation system then reads

$$\underbrace{\begin{pmatrix} \Theta_{ASW} & \Theta_{WW} & \Theta_{WDW} & \Theta_{GMW} \\ S_{AASW} & S_{AWW} & S_{AWDW} & S_{AGMW} \\ DO_{ASW} & DO_{WW} & DO_{WDW} & DO_{GMW} \\ 1 & 1 & 1 & 1 \end{pmatrix}}_{\mathbf{A}} \underbrace{\begin{pmatrix} x_{ASW} \\ x_{WW} \\ x_{WDW} \\ x_{GMW} \end{pmatrix}}_{\mathbf{x}} = \underbrace{\begin{pmatrix} \Theta_{obs} \\ S_{A_{obs}} \\ DO_{obs} \\ 1 \end{pmatrix}}_{\mathbf{b}}, \quad (1)$$

where the constant source water (given by the subscripts) properties, conservative temperature  $\Theta$ , absolute salinity  $S_A$ , and dissolved oxygen  $DO$ , are summarized in the matrix  $\mathbf{A}$ . The fractions of the source water masses are given in the vector  $\mathbf{x}$ , and the observed properties are contained in the vector  $\mathbf{b}$ . The equation in the last row of the system is mass conservation, i.e. the fractions in  $\mathbf{x}$  have to sum up to 1.

$\mathbf{A}$  and  $\mathbf{b}$  were normalized, denoted as  $\mathbf{A}_{norm}$  and  $\mathbf{b}_{norm}$ , respectively, to make the tracers of incomparable units comparable. In addition, the tracers were given different relative weights in the equations, using a diagonal weighting matrix  $\mathbf{W}$ , which



~~contains the weight for each tracer:~~

$$150 \quad \mathbf{W} = \begin{pmatrix} W_{\Theta} & 0 & 0 & 0 \\ 0 & W_{S_A} & 0 & 0 \\ 0 & 0 & W_{DO} & 0 \\ 0 & 0 & 0 & W_{mass} \end{pmatrix}. \quad (2)$$

We set the weights for conservative temperature, absolute salinity, and mass conservation  $W_{\Theta} = W_{S_A} = W_{mass} = 100$  and the weight for dissolved oxygen  $W_{DO} = 1$ . These values were chosen to account for the less reliable absolute values of oxygen and gave the most realistic water mass distributions. The normalized versions of  $\mathbf{A}$  and  $\mathbf{b}$  were then multiplied with  $\mathbf{W}$ :

$$\tilde{\mathbf{A}} = \mathbf{W} \mathbf{A}_{norm} \quad (3)$$

$$155 \quad \tilde{\mathbf{b}} = \mathbf{W} \mathbf{b}_{norm}. \quad (4)$$

The system of equations was solved for  $\mathbf{x}$  by minimizing the residual

$$d = \|\tilde{\mathbf{A}}\mathbf{x} - \tilde{\mathbf{b}}\|_2^2, \quad (5)$$

where the subscript 2 denotes the Euclidean norm, and a non-negativity constraint is imposed on  $\mathbf{x}$  to avoid non-physical fractions of negative  $\mathbf{x}$ . The algorithm by Lawson and Hanson (1974) was then used to solve the linear equation system under this constraint. The OMP analysis was conducted for the mean tracer values during the first year of observations when salinity measurements were available, i.e. until the end of 2010. As no salinity data were available at M3<sub>upper</sub>, the mean value from M1<sub>upper</sub> was assumed due to similar temperature and oxygen values at the two sites. In addition, the OMP analysis was done for daily averages of the tracers at M1<sub>upper</sub> and M2<sub>upper</sub> until the end of 2010. These two instruments were chosen as they revealed more seasonal variability within the first year compared to the other instruments.

165 The source water properties of ASW, WW, and WDW were derived from  $\Theta$ - $S_A$  (Fig. B2) and  $\Theta$ - $DO$  (Fig. 5) diagrams from the auxiliary CTD, mooring, and Winkler titration data described in Sect. 2.2. For GMW, the salinity was set to  $S_{AGMW} = 0 \text{ g kg}^{-1}$ . Its conservative temperature was set to a theoretical value that accounts for heat conduction from water to ice, latent heat transfer, and mixing of meltwater with the ambient water (Jenkins, 1999). This temperature is the x-axis intercept of a meltwater mixing line in  $\Theta$ - $S_A$  space (Gade, 1979). Following Nakayama et al. (2013), Biddle et al. (2017), and Zheng et al. (2021), this effective temperature was set to  $\Theta_{GMW} = -90.8^\circ\text{C}$ . Dissolved oxygen values for GMW have in earlier studies been obtained by extrapolating CDW-GWM mixing lines to a salinity of  $0 \text{ g kg}^{-1}$  in  $\Theta$ - $DO$  space, resulting in a range of  $25 \text{ ml l}^{-1}$  to  $30 \text{ ml l}^{-1}$  (Hellmer et al., 1998; Jenkins, 1999; Jenkins and Jacobs, 2008). Since these meltwater mixing lines are not observed in our mooring data, we set  $DO_{GMW} = 28 \text{ ml l}^{-1}$  for GMW, following the latter and other (Nakayama et al., 2013; Biddle et al., 2017; Wählín et al., 2021) studies. In  $\Theta$ - $DO$  space, meltwater mixing lines were estimated via a straight line to the GMW end member at  $DO_{GMW} = 28 \text{ ml l}^{-1}$  and  $\Theta_{GMW} = -90.8^\circ\text{C}$  (Fig. 5).

The source water masses represent a range rather than a point in  $\Theta$ - $S_A$ - $DO$  space, and the measured variables from the instruments can contain offsets due to drift and accuracy of the sensors. To quantify how much both these factors influence



**Table 2.** End-member values of the source water mass conservative temperature ( $\Theta$ ), absolute salinity ( $S_A$ ), and dissolved oxygen ( $DO$ ), including their uncertainties. The values are based on the water mass distributions in Fig. B1.

	$\Theta$	$S_A$	$DO$
Antarctic Surface Water	$-0.5 \pm 0.5^\circ\text{C}$	$34.15 \pm 0.2 \text{ g kg}^{-1}$	$8 \pm 0.5 \text{ ml l}^{-1}$
Winter Water	$-1.88 \pm 0.1^\circ\text{C}$	$34.45 \pm 0.1 \text{ g kg}^{-1}$	$7.1 \pm 0.3 \text{ ml l}^{-1}$
Warm Deep Water	$0.5 \pm 0.3^\circ\text{C}$	$34.8 \pm 0.05 \text{ g kg}^{-1}$	$4.9 \pm 0.2 \text{ ml l}^{-1}$
Glacial Meltwater	$-90.8 \pm 5^\circ\text{C}$	$0 \pm 0 \text{ g kg}^{-1}$	$28 \pm 5 \text{ ml l}^{-1}$

the results of the OMP analyses, we estimated the propagated uncertainties as described in Appendix B. The properties of all source water masses and their respective ranges are given in Table 2 and visualized in Fig. B1.

## 180 2.4 Thermal wind

The water mass estimates described above were complemented by estimates of horizontal density gradients, derived from the vertical shear of the horizontal velocity **via the thermal wind equation**

$$\frac{\partial \rho}{\partial x} = -\frac{f}{\rho_0 g} \frac{\Delta v}{\Delta z} \quad (6)$$

$$\frac{\partial \rho}{\partial y} = \frac{f}{\rho_0 g} \frac{\Delta u}{\Delta z}, \quad (7)$$

185 where  $\rho$  is the density,  $f = -1.37 \times 10^{-4} \text{ s}^{-1}$  is the Coriolis parameter,  $\rho_0 = 1028 \text{ kg m}^{-3}$  is a reference density,  $g = 9.81 \text{ m s}^{-2}$  is the gravitational acceleration,  $\Delta u$  and  $\Delta v$  are the differences of eastward and northward velocity, respectively, between upper and lower instrument<sub>u</sub> at each mooring, and  $\Delta z$  is the vertical distance between the two instruments. The calculation was done using monthly averaged velocities.

The distance over which the density gradients are valid is the baroclinic Rossby radius of deformation. Following Chelton  
190 et al. (1998), we estimated the first mode of the baroclinic Rossby radius according to

$$R = \frac{1}{|f|\pi} \int_{-H}^{-D} N(z) dz \approx \frac{\Delta z}{|f|\pi} \sum_{i=-H}^{i=-D} N_i \quad (8)$$

where  $H$  is the water depth,  $D$  is the depth of the ice draft,  $z$  is the vertical coordinate,  $\Delta z = 1 \text{ m}$  is the depth increment, and  $N$  is the Brunt-Väisälä frequency, calculated from the CTD profiles obtained at the mooring sites before mooring deployment (Hattermann et al., 2012) using the Gibbs-SeaWater Toolbox (McDougall and Barker, 2011). This yields a baroclinic Rossby  
195 radius of around  **$R = 1\text{-}10 \text{ km}$** .

The magnitude of the velocity difference vector ( $\Delta u$ ,  $\Delta v$ ) between upper and lower instruments (referred to as velocity shear hereafter) serves as a measure of how baroclinic the flow is, i.e. **how large** the depth-varying component of the flow **is**. A small and large magnitude indicate weaker and stronger baroclinic conditions, respectively.





## 2.5 Warm events

200 As inflows of WDW into the cavity at  $M1_{\text{lower}}$  are of particular interest for basal melting at Fimbulisen (Lauber et al., 2023c), we investigated the oceanic conditions before, during, and after such warm events. There were 1767 hourly measurements of temperatures above a threshold of  $-1.39^{\circ}\text{C}$  (the long-term mean plus three standard deviations) at  $M1_{\text{lower}}$ . These measurements were split into 189 individual warm events, separated by periods when the temperature dropped below the threshold for at least one hourly measurement. The median duration (upper/lower quartile) of individual events was 4 (10/2) hours, and the longest consecutive inflow event lasted for 96 hours (Fig. C1a).

To investigate the cavity hydrography and circulation associated with the warm events, composites of the evolution of temperature, oxygen, and velocity from ten days before to ten days after all warm events were computed. For that purpose, hourly time series before the warm events were aligned to the first record of each event above the threshold and averaged across all events. Likewise, hourly time series after the warm events were aligned with the last record of each event above the threshold and averaged across all events. All values during the warm events were averaged into one value at zero offset. The time of zero offset is referred to as  $t_0$  hereafter. When warm events were separated by less than ten days, the composite averages contained autocorrelations. To minimize the effect of these, other warm events occurring within ten days before or after a warm event were excluded from the respective average. To assess the robustness of the composite averages, significances and uncertainties were calculated as described in Appendix C.

## 215 3 Results

### 3.1 Mooring observations

The up to 12 year long temperature, oxygen, and velocity records from all six mooring instruments are presented in Fig. 2. At the upper instruments, 82 % of all temperature measurements are lower than the surface freezing point of  $-1.88^{\circ}\text{C}$  (Fig. 2a-c). This shows the presence of buoyant ISW, commonly found close to the ice base due to freshwater input from GMW (Nøst and Foldvik, 1994). Oxygen values range from  $7\text{ml}^{-1}$  to  $8\text{ml}^{-1}$ . At  $M1_{\text{upper}}$  and  $M3_{\text{upper}}$ , temperatures reach a maximum of about  $-1.3^{\circ}\text{C}$  every year, coinciding with oxygen maxima of up to  $8.1\text{ml}^{-1}$  (Fig. 2a/c). These temperature and oxygen maxima can be attributed to shallow intrusions of ASW in autumn below the ice drafts shallower than 190 m (Hattermann et al., 2012). The velocities at  $M1_{\text{upper}}$  and  $M3_{\text{upper}}$  are predominantly directed southward into the cavity with mean speeds of around  $5\text{cm s}^{-1}$ . At  $M2_{\text{upper}}$ , temperature maxima (up to  $-1.8^{\circ}\text{C}$ ) and minima (down to  $-2.1^{\circ}\text{C}$ ) are lower than at  $M1_{\text{upper}}$  and  $M3_{\text{upper}}$  (Fig. 2b), consistent with less influence of ASW and a lower in situ freezing point below the 350 m deep ice draft. At the same time, oxygen background values at  $M2_{\text{upper}}$  are around  $0.2\text{ml}^{-1}$  lower than at  $M1_{\text{upper}}$  and  $M3_{\text{upper}}$ , and maxima remain below  $7.6\text{ml}^{-1}$ . The velocity at  $M2_{\text{upper}}$  is predominantly directed toward the northeast along the basal channel at a speed of around  $2\text{cm s}^{-1}$ .

At the lower instruments, 91 % of temperature observations lie above the surface freezing point, with oxygen values around  $7\text{ml}^{-1}$  (Fig. 2d-f). Temperature maxima reach  $0^{\circ}\text{C}$  at  $M1_{\text{lower}}$ ,  $-1.3^{\circ}\text{C}$  at  $M2_{\text{lower}}$ , and  $-1.5^{\circ}\text{C}$  at  $M3_{\text{lower}}$ . These maxima



are accompanied by a decrease in oxygen down to  $5.3 \text{ ml l}^{-1}$  and can be attributed to intrusions of WDW or modified WDW (mWDW, a mixture between WW and WDW) into the cavity at depth (Hattermann et al., 2012; Lauber et al., 2023c). At all lower instruments, minimum temperatures of down to  $-1.99^\circ\text{C}$  are observed in May/June in the years 2014 to 2016, indicating the presence of ISW in the lower part of the cavity. ~~Until~~ 2014, mean velocities at  $M1_{\text{lower}}$  remain below  $2 \text{ cm s}^{-1}$  and  
235 vary in direction (Fig. 2d). Afterward, the flow direction at  $M1_{\text{lower}}$  alternates seasonally between northwestward (out of the cavity) and southeastward (into the cavity) at mean speeds of up to  $8 \text{ cm s}^{-1}$ . At  $M2_{\text{lower}}$ , a near-continuous eastward flow of around  $2 \text{ cm s}^{-1}$  roughly follows bathymetric contours into the cavity (Fig. 2e). At  $M3_{\text{lower}}$ , the flow is southwestward along bathymetric contours at speeds around  $4 \text{ cm s}^{-1}$  (Fig. 2f). This shows that mWDW also enters the cavity at the eastern sill as previously hypothesized by Nicholls et al. (2006).

240

To assess patterns of seasonal temperature variability, we examine the frequency of occurrence of different temperature intervals during each month, with red lines indicating percentiles of the monthly varying temperature distribution (Fig. 3).

At  $M1_{\text{upper}}$  and  $M3_{\text{upper}}$ , a pattern of higher temperatures is more frequently observed from December to May, showing the arrival of solar-heated ASW after it has been ~~suppressed~~ below the depths of the ice shelf draft in autumn (Fig. 3a/c, Zhou  
245 et al., 2014). This variability is also reflected in the mean and all shown percentiles, which resemble the consistent seasonal variability of the respective full time series (Fig. 2a/c). At  $M2_{\text{upper}}$ , we observe a somewhat reversed temperature seasonality (Fig. 3b): from April to June, the more frequent occurrence of temperatures below  $-2^\circ\text{C}$  indicates higher ISW concentrations during this period. During the rest of the year, the mean temperature is around  $-1.95^\circ\text{C}$ .

At  $M1_{\text{lower}}$ , the most commonly observed temperatures lie around the surface freezing point throughout the year, with 64 %  
250 of all hourly temperature observations ranging between  $-1.8^\circ\text{C}$  and  $-1.9^\circ\text{C}$  (Fig. 3d). The monthly temperature distributions at  $M1_{\text{lower}}$  show a long tail toward high values, corresponding to WDW. This tail is most pronounced between January and March and between September ~~to~~ November, as shown by the 80 % and 99 % percentiles. Between May and August, such high-temperature excursions are less frequent, and temperatures below the surface freezing point are more frequent. This is also seen in the 1 % percentile and indicates the presence of ISW. In summary, the temperature distribution at  $M1_{\text{lower}}$  is the  
255 result of the superposition of three different modes: (i) a constant background temperature at the surface freezing point, (ii) warm mWDW/WDW presence in (a) January to March and (b) September to November, and (iii) cold ISW presence between May and August.

At  $M2_{\text{lower}}$ , all three modes from  $M1_{\text{lower}}$  are evident (Fig. 3e). This similarity is ~~in-line~~ with the regional proximity of the two sites and their ~~connectivity along~~ contours of constant water column thickness. mWDW is generally colder, and ISW is  
260 warmer at  $M2_{\text{lower}}$  than at  $M1_{\text{lower}}$ . At  $M3_{\text{lower}}$ , the same three modes are present, but two of them are somewhat modified (Fig. 3f): mWDW is observed predominantly between February and April, and ~~much~~ limited during the rest of the year. In addition, ISW occurs between March and May, i.e. around two months earlier than at  $M1_{\text{lower}}$  and  $M2_{\text{lower}}$ .

To investigate the seasonal variability in velocities and their connections to the temperature, monthly mean arrows of the observed velocities and associated variance ellipses are shown in Fig. 4.

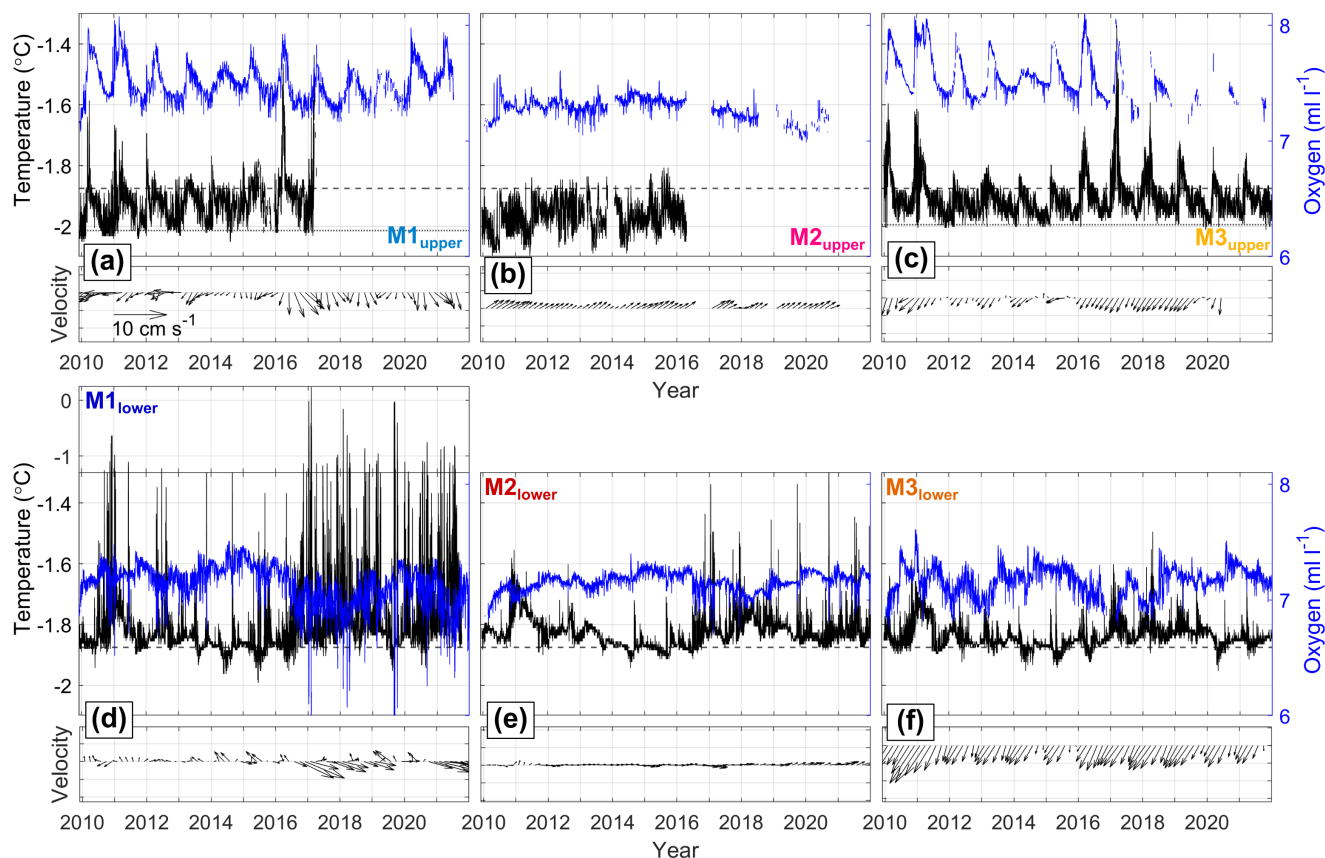


**Figure 2.** Time series of hourly in situ temperature (left axis, black), daily dissolved oxygen (right axis, blue), and 60-day binned and four-bin (=240 days) filtered horizontal velocity (black arrows) at (a) M1<sub>upper</sub>, (b) M2<sub>upper</sub>, (c) M3<sub>upper</sub>, (d) M1<sub>lower</sub>, (e) M2<sub>lower</sub>, (f) M3<sub>lower</sub>. The freezing temperature for water at a reference salinity of 34.4 g kg<sup>-1</sup> at surface pressure (dashed line) and the depth of the ice base (dotted line in upper instrument time series, Table 1) are indicated. At M2<sub>upper</sub>, the in situ freezing temperature of -2.14 °C, lies outside of the shown temperature range.

265 At M1<sub>upper</sub>, the velocities reach a maximum speed of 4 cm s<sup>-1</sup> in south-southwest direction in April (Fig. 4a). This shows that the ASW observed during this time (Fig. 3a) intrudes the cavity along the western side of the Jutulstraumen keel (Fig. 1b). After July, increased velocity variability across the keel coincides with the absence of ASW. Similar to M1<sub>upper</sub>, the current speed at M3<sub>upper</sub> is at a maximum of 4 cm s<sup>-1</sup> toward the southwest in March when ASW is observed (Fig. 4c and 3c). At M2<sub>upper</sub>, highest speeds of 3 cm s<sup>-1</sup> toward the northeast are observed together with the coldest temperatures in May (Fig. 270 4b and 3b). This coincidence of strong currents and low temperatures supports the picture of a buoyancy-driven flow, where ISW has been freshened along a meltwater mixing line, decreasing its density and hence rising faster along the ice base. The northeastward direction of the flow and its relatively small variability at M2<sub>upper</sub> aligns with the basal channel in which the instrument is located, and which seems to guide ISW from west to east across the Jutulstraumen keel at this location.

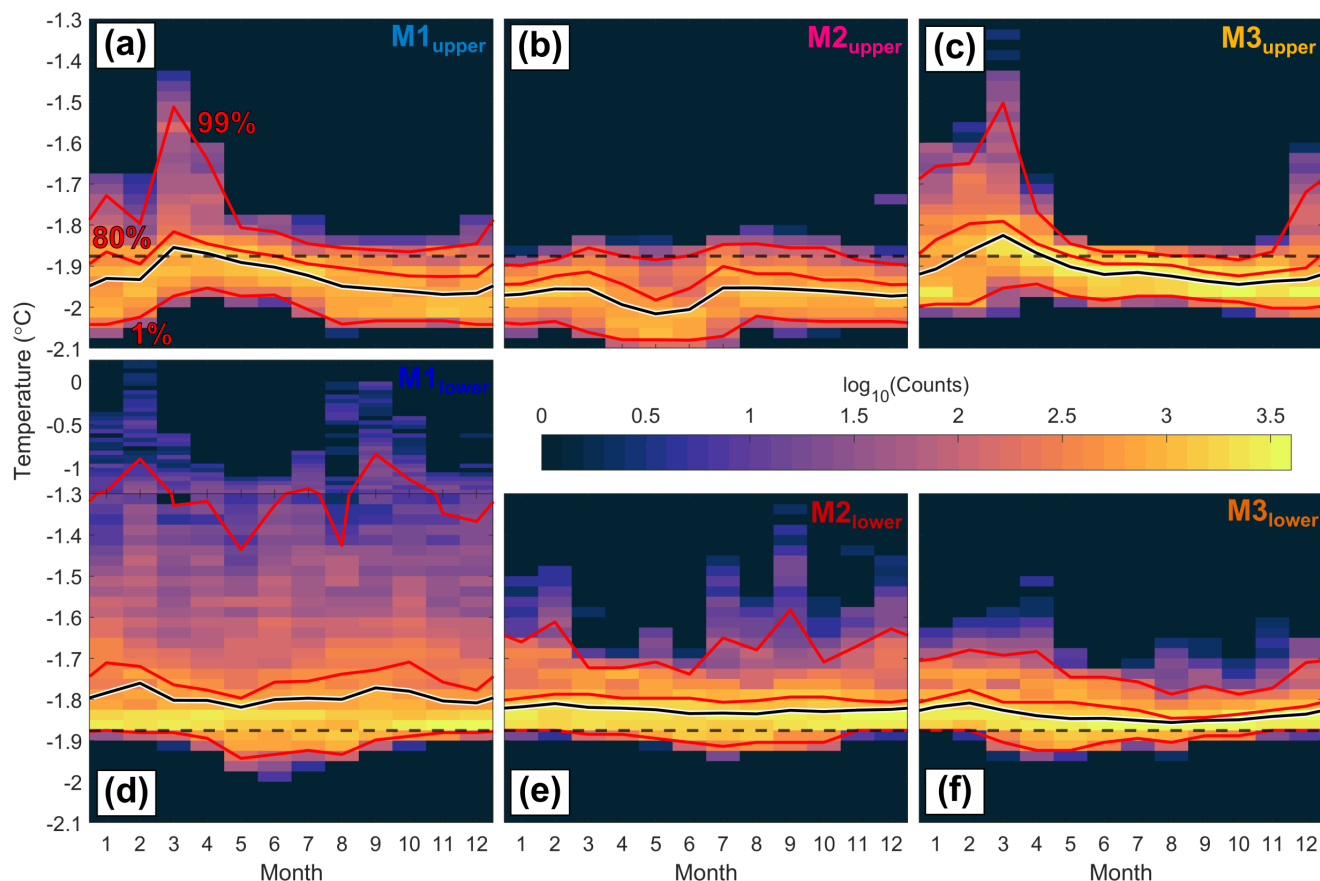


**Figure 3.** Histograms of hourly temperature observations binned into month-temperature intervals at (a)  $M1_{upper}$ , (b)  $M2_{upper}$ , (c)  $M3_{upper}$ , (d)  $M1_{lower}$ , (e)  $M2_{lower}$ , (f)  $M3_{lower}$ . The black lines are the mean temperature and the red lines are the 1%, 80%, and 99% percentiles during the respective month. The black horizontal dashed lines indicate the surface freezing point for a salinity of  $34.4 \text{ g kg}^{-1}$ .

At  $M1_{lower}$ , the velocity is directed toward the northwest (out of the cavity) at a mean speed of  $4 \text{ cm s}^{-1}$  from April to June, and toward the southeast (into the cavity) at a mean speed of up to  $4 \text{ cm s}^{-1}$  from September to January (Fig. 4d). The timing of the outflow coincides with the lowest temperatures (Fig. 3d), i.e. ISW flows out of the cavity. The timing of the inflow coincides with the period when the highest temperature excursions are observed and no ISW is present. The flow at  $M2_{lower}$  does not seasonally reverse its direction as at the main sill, but the eastward velocity is strongest at  $3 \text{ cm s}^{-1}$  in November (Fig. 4e) when the inflow at  $M1_{lower}$  is close to strongest. This supports the connectivity between the  $M1_{lower}$  and  $M2_{lower}$  locations within the cavity. At  $M3_{lower}$ , the southwestward (into the cavity) velocity reaches a maximum of  $5 \text{ cm s}^{-1}$  from April to June (Fig. 4f). The inflow is weakest in September and October, similar to the flow below the ice base at  $M3_{upper}$  (Fig. 4c). That is, the seasonal variability in the deep hydrography and currents at the main sill is different from that at the eastern sill and will be further investigated in Sect. 4.1.

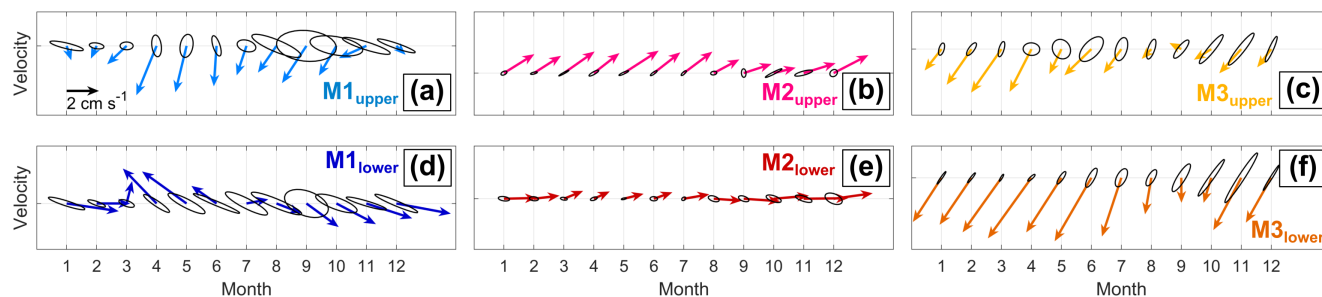


**Figure 4.** Monthly climatology and variance ellipses of horizontal velocity at (a) M1<sub>upper</sub>, (b) M2<sub>upper</sub>, (c) M3<sub>upper</sub>, (d) M1<sub>lower</sub>, (e) M2<sub>lower</sub>, (f) M3<sub>lower</sub>. For clarity, the size of the variance ellipses has been divided by a factor of two in all panels. The reference arrow in panel a is valid for all panels. Up = northward, right = eastward.

### 3.2 Water mass distribution

285 The water masses inside the Fimbulisen cavity and on the continental slope are characterized in a  $\Theta$ - $DO$  diagram in Fig. 5. The three auxiliary data sets (introduced in Sect. 2.2) show a pronounced mixing line at a constant slope between warm/oxygen-poor WDW and cold/oxygen-rich WW, which is the most abundant water mass at all sub-ice-shelf instruments. This mixing line is also present in the data from the lower sub-ice-shelf instruments. Therefore, the mixing line was utilized to remove noise and a systematic offset of  $0.4 \text{ ml l}^{-1}$  in the lower sub-ice-shelf data compared to the auxiliary data (details described in  
290 Appendix A).

ASW is characterized by a higher dissolved oxygen concentration than WDW and WW and generally represents a broader range of water mass properties than WDW (Fig. B1). Mixing of WW and ASW does therefore not happen along a clear line in  $\Theta$ - $DO$  space (Fig. 5). Hence, no distinct offset between the upper sub-ice-shelf data and auxiliary data was identified in  $\Theta$ - $DO$  space, but instead in  $S_A$ - $DO$  space (Fig. A1), giving the same offset of  $0.4 \text{ ml l}^{-1}$  as for the lower instruments (details described in  
295 Appendix A). The signatures of ISW at the upper instruments show that GMW has been added after the interaction of a water mass above the surface freezing point with the ice base. In  $\Theta$ - $DO$  space, the addition of GMW cools and adds oxygen to a water mass. As such, following meltwater mixing lines, the ISW observed at the upper instruments can be traced back to originate from ice shelf melting by ASW and WW and consequent mixing with GMW (Fig. 5).

We apply the OMP analysis to quantify the mean concentrations of the source water masses at the instrument sites during  
300 2010 (when good salinity data were available at all instruments except M3<sub>upper</sub>). The results are visualized in pie charts in Fig. 1b and the respective values are given in Table 3: WW dominates the water mass composition at all instruments with concentrations between 78 % and 97 %. More ASW is observed at M3<sub>upper</sub> (22 %) than at M1<sub>upper</sub> (13 %), despite their similar ranges in  $\Theta$ - $DO$  space (Fig. 5). At M2<sub>upper</sub>, a lower ASW concentration (6 %) is consistent with the instrument's location below a deeper ice draft (350 m) than M1<sub>upper</sub>/M3<sub>upper</sub> (190 m/160 m). GMW is at a level of 0.2 % to 0.3 % at all

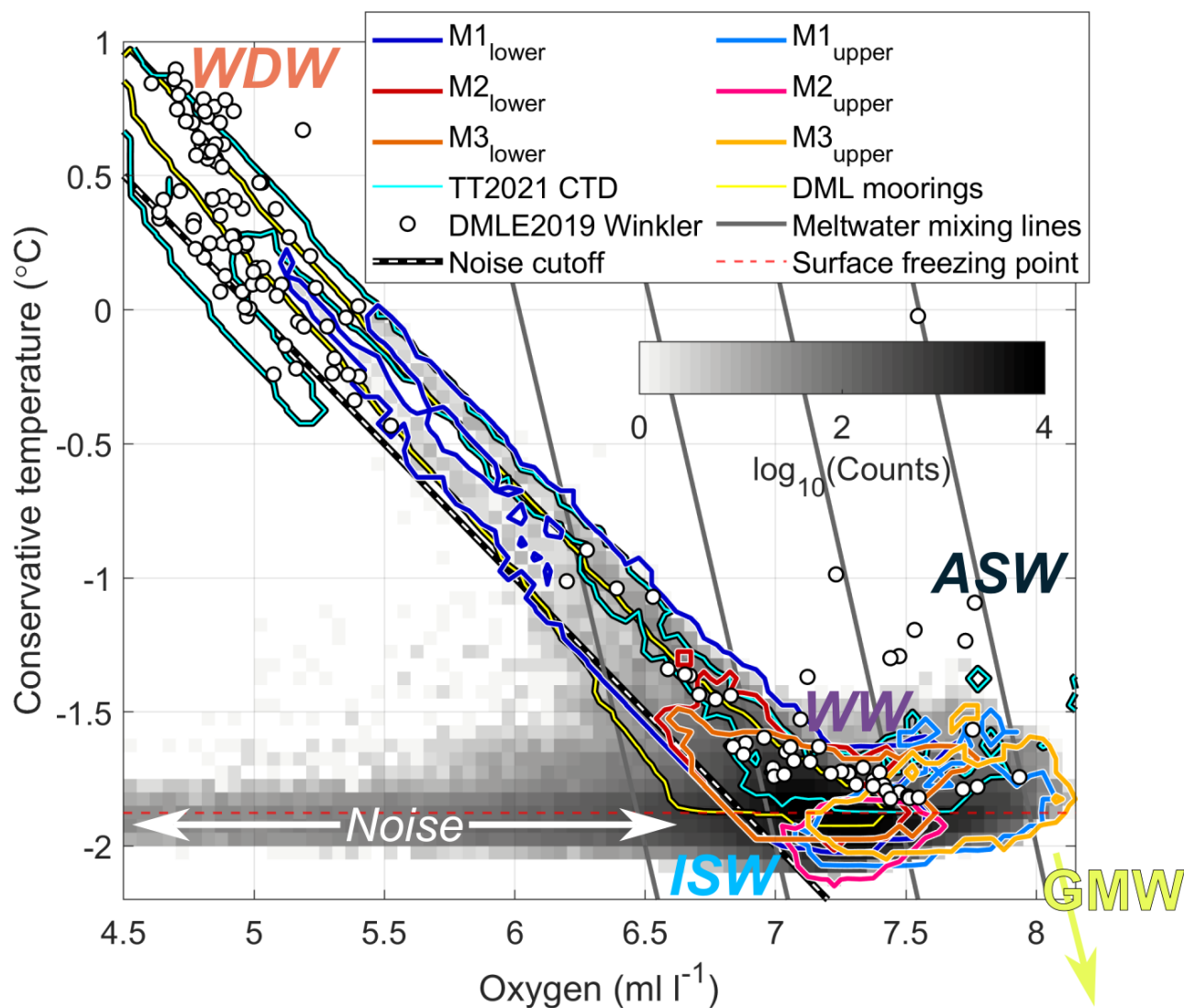


**Figure 5.** Conservative temperature - dissolved oxygen diagram of the sub-ice-shelf mooring data and auxiliary data. The gray shading is a histogram of all hourly upper and lower mooring data (offset removed, noise not removed). Colored lines show the range of the single mooring instruments (blue, red, orange, 1 count contour, noise removed) of the DML<sub>deep</sub>/DML<sub>shallow</sub> mooring data (yellow, 5 counts contour) and of the Troll Transect 2020/21 CTD data (cyan, 5 counts contour). White dots show oxygen concentrations obtained from Winkler titration and temperature from CTD stations during the Southern Ocean Ecosystem cruise 2019. The gray lines are meltwater mixing lines and the black/white dashed line is the threshold below which the oxygen data from the lower sub-ice-shelf mooring instruments are considered noise. The horizontal red dashed line indicates the surface freezing point for a salinity of 34.4 g kg<sup>-1</sup>.



**Table 3.** Mean percentages of water mass distribution at M1-3 during 2010 shown in the pie charts in Fig. 1b from the Optimum Multiparameter analysis (see Methods)

	M1 <sub>upper</sub>	M1 <sub>lower</sub>	M2 <sub>upper</sub>	M2 <sub>lower</sub>	M3 <sub>upper</sub>	M3 <sub>lower</sub>
Antarctic Surface Water	13.1 ± 12.6	0 ± 7.9	5.7 ± 9.3	0 ± 7.4	22.0 ± 15.0	14.3 ± 11.8
Winter Water	86.6 ± 13.8	97.2 ± 9.2	94.1 ± 11.6	97.0 ± 9	77.7 ± 16.8	81.3 ± 14.7
Warm Deep Water	0 ± 3.9	2.8 ± 5.5	0 ± 5.7	3 ± 5.6	0 ± 4.2	4.1 ± 7.8
Glacial Meltwater	0.3 ± 0.2	0 ± 0.1	0.2 ± 0.2	0 ± 0.1	0.3 ± 0.2	0.3 ± 0.3

305 upper instruments, comparable to estimates of around 0.5 % in front of Fimbulisen at the depth of the ice draft (Price et al., 2008). No traces of WDW are observed at the upper instruments **in the mean state** during 2010.

At the lower instruments, WW concentrations of at least 81 % are related to the first mode of the temperature distributions (Fig. 3d-f), i.e. temperatures at the freezing point (as introduced in Sect. 3.1). The WDW concentration is between 3 % and 4 %, related to the second mode. As the WDW is mixed with WW, it is strongly modified WDW that is continuously present  
 310 inside the cavity. During warm events, however, when the highest temperatures and lowest oxygen values are observed (Fig. 2d), the WDW concentrations at M1<sub>lower</sub> are expected to reach close to 100 % (Fig. 5). A high ASW concentration of 14 % is seen at M3<sub>lower</sub>, associated with an exceptional ASW inflow event at the end of 2010. Such an event ~~is not repeatedly observed~~ in the temperature and oxygen time series ~~during~~ the remaining 11 years (Fig. 2f), implying that a mean ASW concentration of 14 % is an overestimate after 2010. No GMW is found at M1<sub>lower</sub>/M2<sub>lower</sub> **in the mean state during 2010**, but 0.3 % at M3<sub>lower</sub>,  
 315 similar to the upper instruments.

The temporal evolution of the water mass composition during 2010 at M1<sub>upper</sub> is shown in Fig. 6a: in December, the beginning of summer, WW accounts for nearly 100 % of the observed water mass composition, with an admixture of 0.2 % GMW. From mid-February to mid-March, the ASW fraction rapidly increases to a maximum of 75 %, while the WW fraction  
 320 reduces to 20 %. At the same time, the GMW concentration increases by an order of magnitude to 1.3 %, which gives evidence of increased ice shelf melting due to the presence of warm ASW. The ASW presence coincides with an increase ~~of~~ the WDW fraction, but the magnitude of the latter is five times smaller than its uncertainty and may originate from the OMP method detecting a portion of ASW as WDW due to ~~similar~~ temperature signatures of the two water masses, rather than being a robust signal. After March, a decrease in the ASW and GMW fractions and an increase in the WW fraction happen ~~slower~~ than the  
 325 changes before March. Between October and December, the water mass ~~consists again~~ almost ~~fully~~ of WW.

At M2<sub>upper</sub> (Fig. 6b), the water mass evolution differs from that at M1<sub>upper</sub>: the WW concentration is close to 100 % from January to April, with only occasional contributions of ASW, WDW, and GMW below 5 % during this period. **The occurrence of WDW traces below the ice base at M2<sub>upper</sub>** provides evidence **of the overturning circulation inside the cavity** (Nøst and Foldvik, 1994). Such overturning occurs when WDW enters the cavity at the seafloor, causes melting at deeper parts of the

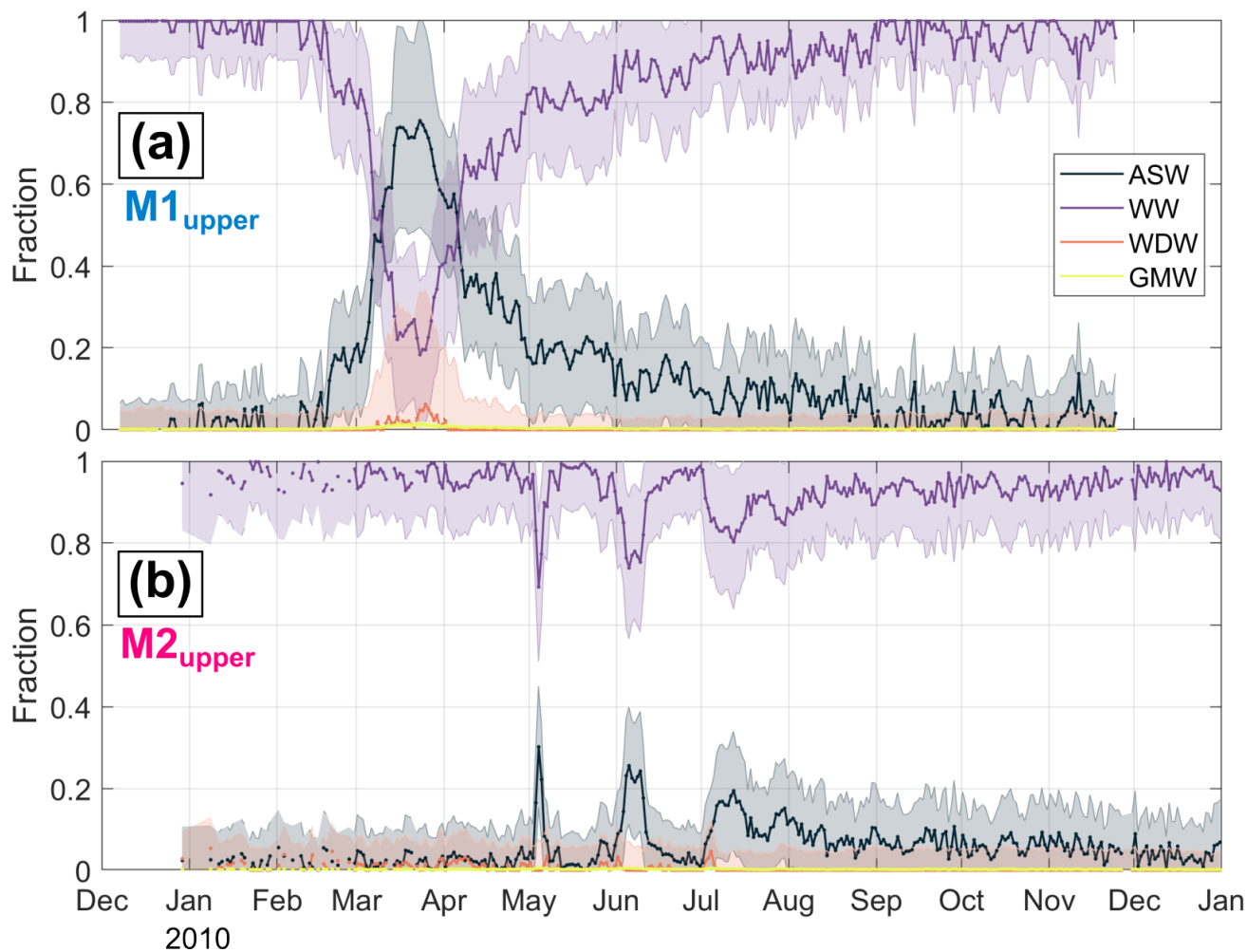


**Figure 6.** Time series of water mass fractions of the source water masses defined in Table 2, derived from Optimum Multiparameter analysis (see Methods) for (a)  $M1_{upper}$ , (b)  $M2_{upper}$ . Envelopes indicate the uncertainty (see Appendix B).

330 ice shelf, and rises along the ice base as it gains buoyancy from the GMW input. In  $\Theta$ -DO space (Fig. 5), the influence of WDW below the ice base is indicated by a meltwater mixing line connecting the low-oxygen water mass at  $M2_{upper}$  to the WDW-WW mixing line up to a temperature of  $-1.3^{\circ}\text{C}$ . In May and June, the ASW fraction increases to 30 % during two five- and ten-day-long pulses, together with an increase of the GMW concentration to around 0.6 %. In July, ASW again increases to 20 %, but slowly decreases over the following six months. This shows that with a three-month delay compared to  $M1_{upper}$ ,  
 335 ASW can reach below a 350 m deep ice draft and as far into the cavity as  $M2_{upper}$  in winter. This delay is consistent with the wind-driven deepening of ASW at the ice front in autumn/winter over the timescale of months (Zhou et al., 2014). During the ASW decrease after July, WW again increases, and no WDW is detected anymore, possibly being replaced by the ASW.





Due to the lack of good salinity data, the water mass composition cannot be quantified after 2010. However, at M1<sub>upper</sub>, temperature (Fig. 3a) and oxygen (Fig. A2) maxima around March/April imply that the water mass evolution shown in Fig. 6a is generally valid for the whole 12 year long time series. At M3<sub>upper</sub>, coinciding temperature (Fig. 3c) and oxygen (Fig. A2) maxima and absolute values (Fig. 5) compared to M1<sub>upper</sub> show that hydrographic conditions at the two sites are comparable. We also note coinciding maxima in the long-term mean oxygen at M2<sub>upper</sub> and M3<sub>lower</sub> in July (Fig. A2), indicating that traces of ASW reach down to M2<sub>upper</sub> at 370 m depth and even to M3<sub>lower</sub> at 450 m depth every year.

Oxygen values at M2<sub>upper</sub> decrease by around 0.25 ml l<sup>-1</sup> after 2016 when no corresponding temperature measurements are available anymore (Fig. 2b). We cannot exclude that this signal is related to sensor drift, but it may also provide evidence of the impacts of enhanced warm inflows observed during that time: the lower oxygen values at M2<sub>upper</sub> indicate a source water mass that is located on a mixing line further left in Fig. 5, implying a larger fraction of mWDW (note that maintaining the observed oxygen decreases by 0.25 ml l<sup>-1</sup> without changing the source water composition would imply an unrealistic temperature increase of 1 °C along a mixing line (Fig. 5)). A higher WDW fraction in the ISW at M2<sub>upper</sub> after 2016 is consistent with an enhanced contribution of WDW to basal melting of deeper parts of the ice shelf and a rise of the derived ISW along the ice base, as proposed by Lauber et al. (2023c). To corroborate this relationship, we adjusted the temperature and oxygen values in the mean OMP analysis to the mean values after 2016 for M1<sub>lower</sub> (neglecting changes in salinity) and M2<sub>upper</sub> (neglecting changes in salinity and temperature). This estimate yields an increase in WDW concentration from 2.8 % to 6.7 % at M1<sub>lower</sub> and from 0 % to 7.2 % at M2<sub>upper</sub>. This change is comparable at the two sites, supporting that the enhanced inflow of WDW at the main sill after 2016 increased the presence of WDW-derived ISW at M2<sub>upper</sub>.

### 3.3 Dynamic structure in the cavity

#### 3.3.1 Density gradients

In order to investigate seasonal variations in the spatial distribution of the water masses in the cavity, we estimate the velocity shear and infer the local density gradients at the three sites (Fig. 7) from thermal wind balance (Eqn. 6 and 7). Density gradients obtained this way are assumed to be valid over length scales larger than the baroclinic Rossby radius of  $R = 1\text{-}10\text{ km}$ . The density difference between the water masses in the cavity is larger between ASW and WW ( $\approx 0.5\text{ kg m}^{-3}$ ) and ISW and WW ( $\approx 0.1\text{ kg m}^{-3}$ ) than between WW and mWDW ( $\approx 0.05\text{ kg m}^{-3}$ , Hattermann et al., 2012). Therefore, large density gradients imply that ASW and/or ISW are present close to the ice base. Based on changes in the direction and magnitude of the density gradients, we separate the following description into August to February and March to July, and define two phases in Sect. 3.3.2.

From August to February, the velocity shear remains below 10 cm s<sup>-1</sup> for 92 % of all measurements across all three sites, indicating relatively weak baroclinic conditions (Fig. 7a/c/e). At M1, the velocity at the upper instrument is directed southwestward, and at the lower instrument southeastward (Fig. 4a/d). This is associated with a northward density gradient, i.e. denser water north of the M1 site (Fig. 7b). At M2, the density gradient is northeastward and has a three times smaller magnitude

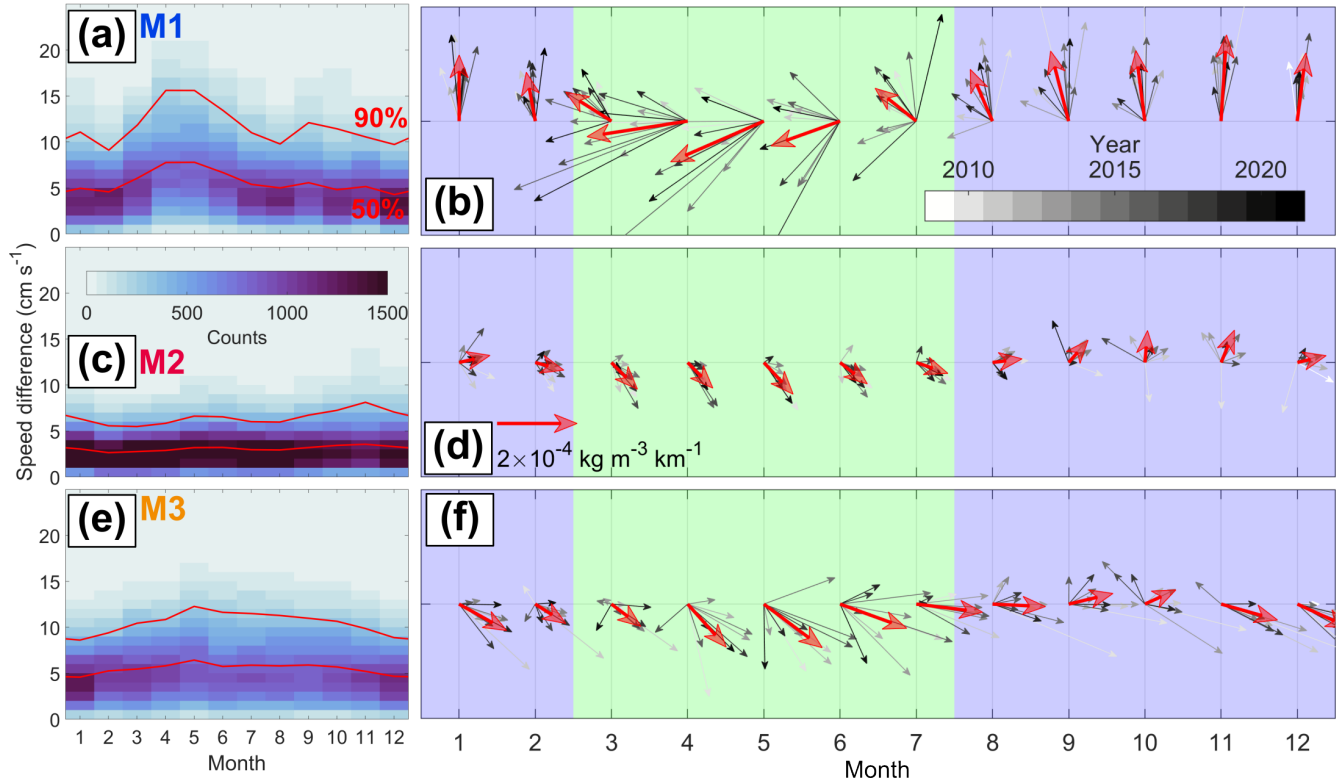


**Figure 7.** Histograms of hourly velocity shear binned on monthly intervals for (a) M1, (c) M2, and (e) M3. The velocity shear is defined as the magnitude of the velocity difference vector ( $\Delta u$ ,  $\Delta v$ ) between the upper and lower instrument and is therefore greater or equal to zero. The red lines are the 50 % and 90 % percentiles during the respective month. Horizontal density gradients estimated from Eqn. 6 and 7 using the velocity difference between the upper and lower instruments at (b) M1, (d) M2, and (f) M3. The bold red arrows are the long-term monthly averages, and thin gray-scale arrows are the monthly averages of individual years as indicated by the colorbar. Green and blue shading marks the two periods sketched in Fig. 8. The reference arrow in panel d is also valid for panels b and f.

370 compared to M1 (Fig. 7d). Density gradients at this site may also be affected by the local flow in the 1 km wide basal channel that M2<sub>upper</sub> is located in. At M3, the gradient is eastward and ~~two times smaller compared to~~ M1 (Fig. 7f).

From March to July, the velocity shear increases to values of up to 15 cm s<sup>-1</sup> to 20 cm s<sup>-1</sup> at M1 and M3, showing an increase in baroclinicity during this period (Fig. 7a/e). At M2, no significant increase in velocity shear is observed (Fig. 7c). The density gradient at M1 rotates toward the west-southwest after February, reaching a maximum in April and May (Fig. 7b).  
 375 During the same months, the density gradients at M2 and M3 are maximum and directed southeastward (Fig. 7d/f).

### 3.3.2 Seasonal phases

The changes in the baroclinicity and density gradients suggest that the cavity circulation alternates between two phases throughout the year. We now describe these two phases by including the previously presented findings (Fig. 8).



From August to February (Fig. 8a), ISW is abundant close to the ice base (Fig. 3a-c), and the shallow inflow of open-ocean  
380 water masses is limited (Fig. 4a-c). The density gradients (Fig. 7b/d/f) suggest a front between lighter ISW inside the cavity  
and denser WW toward the ice front. At the same time, the velocity at the main sill is directed into the cavity (Fig. 4d), and the  
temperature distributions at  $M1_{lower}$  and  $M2_{lower}$  show more frequent inflows of mWDW/WDW (Fig. 3d-e). **Traces of WDW**  
**derived at  $M2_{upper}$**  (Fig. 6b) confirm the contribution of this water mass to basal melting, presumably happening at greater  
depth further inside the cavity. Assuming a velocity of  $2\text{ cm s}^{-1}$  along bathymetric contours at  $M2_{lower}$  (Fig. 4e) and a length  
385 scale of 200 km (Fig. 1a), enhanced intrusions of WDW at the main sill between January and March may indeed explain the  
cooling and acceleration of the ISW two to four months later at  $M2_{upper}$  (Fig. 3b and 4b), implying a strengthening of the  
WDW-driven cavity overturning during this period.

From March to July (Fig. 8b), ASW enters the cavity close to the ice base (Fig. 3a-c and 6). The derived density gradients  
at M1 and M2 (Fig. 7b/d) and velocity at  $M1_{upper}$  (Fig. 4a) indicate that ASW intrudes the cavity along ice draft contours  
390 below the western side of the Jutulstraumen keel and increases the baroclinic circulation inside the cavity. This is consistent  
with modeling results from Hattermann et al. (2014). As ASW is generally lighter than ISW (Hattermann et al., 2012), we  
expect the ASW to act as a wedge between the ice base and ISW, displacing the latter to greater depths. This provides a  
possible explanation for the occurrence of ISW at all lower instruments one to three months after ASW is observed at the  
upper instruments (Fig. 3). At the same time, the presence of ASW at the ice base increases the thermal forcing and, therefore,  
395 the potential for basal melting. Below the relatively shallow ice at  $M1_{upper}$  and  $M3_{upper}$  (190 m and 160 m, respectively),  
melting is **mainly** enhanced by the excess heat of the ASW from solar heating (i.e. ASW temperatures above the surface  
freezing point), as is confirmed by the increase in GMW fraction when ASW is present (Fig. 6a). At the 350 m deep ice draft of  
 $M2_{upper}$ , another effect comes into play: although the traces of ASW arriving at this site have depleted most of the solar heat  
(presumably due to melting and mixing with WW), its temperatures around the surface freezing point (Fig. 3b) still exceed the  
400 local freezing point by  $0.3^\circ\text{C}$ , replacing the colder ISW that had reached its seasonal temperature minimum at this site before  
the arrival of the ASW. The distance from the ice front to  $M2_{upper}$  is about **70 km** via M1 and 150 km via M3. Although the  
exact pathway of ASW to  $M2_{upper}$  remains unclear, the coinciding oxygen maxima in July (Fig. A2) at  $M3_{lower}$  (450 m depth)  
and  $M2_{upper}$  (370 m depth) indicate that a larger portion of the deeper ice of Fimbulisen may be influenced by this water mass.

### 3.4 Characteristics of warm events at $M1_{lower}$

405 Warm events at depth, i.e. the second mode of the  $M1_{lower}$  temperature distribution, have been associated with increased basal  
melting of Fimbulisen (Lauber et al., 2023c) and hence require particular attention. To understand the dynamics of these warm  
events at the main sill, we characterize their temporal evolution at  $M1_{lower}$  and  $M1_{upper}$  by constructing composite averages of  
all 189 recorded warm events during the 12 year long record. A warm event is defined as a period of subsequent measurements  
of hourly temperatures above  $-1.39^\circ\text{C}$  at  $M1_{lower}$ , and the time of the event is referred to as  $t_0$  (see Sect. 2.5 for details).

410 Changes in velocity at  $M1_{lower}$  associated with a warm event are visualized in a hodograph (showing the tip of the composite  
velocity vector from six days before to six days after  $t_0$ , Fig. 9a): starting around three days before and ending around two days  
after  $t_0$ , the velocity signature follows an anticlockwise rotating ellipse with a maximum speed of  $10 \pm 7\text{ cm s}^{-1}$  toward the

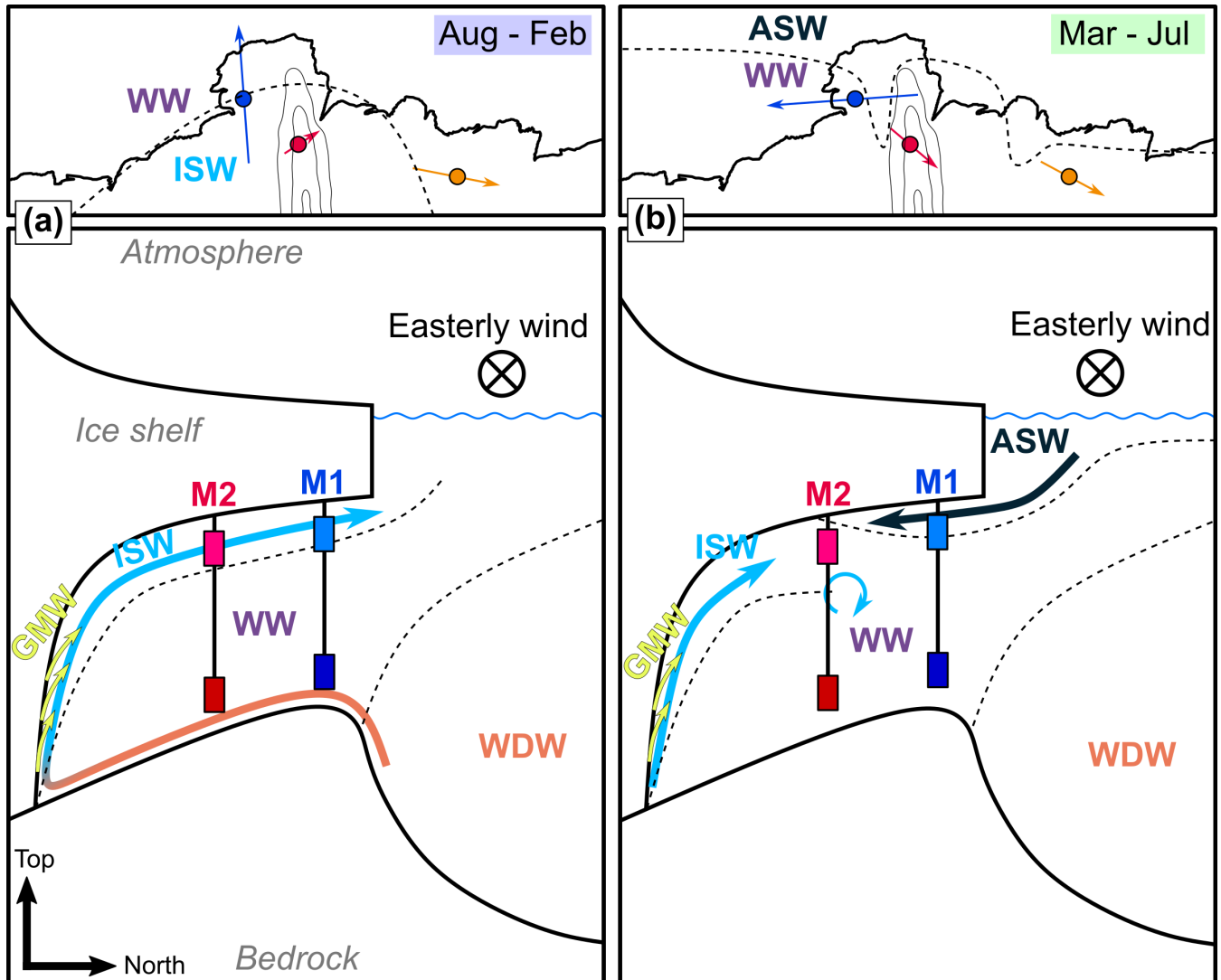


**Figure 8.** Sketches of the estimated water mass distribution at Fimbulisen in (a) August-February and (b) March-July. The upper panels are schematic maps (valid for the upper 100 m of the water column), where the thick black line shows the ice front (Mouginot et al., 2017) and the thin black lines show the smoothed 250, 300, and 350 m contours of the ice draft (Morlighem et al., 2020). Colored arrows at the mooring locations show the mean density gradient from Fig. 7 during the respective period. Dashed lines roughly separate the water masses. The lower panels are north-south cross-sections. The locations of M1 and M2 are indicated, but the relative depth of the instruments is not to scale.

southeast, i.e. into the cavity, at  $t_0$ . The corresponding composite temperature increases from  $-1.7 \pm 0.1^\circ\text{C}$  to a maximum of  $-1.1 \pm 0.3^\circ\text{C}$ , which is at  $t_0$  by definition. Oxygen decreases by  $0.6\text{ml l}^{-1}$  during the same time (Fig. C1c). This observed co-  
 415 varying signal of rotating velocity vector and rapid change in hydrography is the typical signature of a coherent eddy advected



past a mooring (Lilly and Rhines, 2002). Following Lilly and Rhines (2002), we can quantify the following mean properties of these eddies based on the composite velocity time series at  $M1_{\text{lower}}$  around  $t_0$ : a radius of  $r = 8$  km, a half-duration  $\Delta t = 29$  h, an azimuthal speed of  $v_r = 4 \text{ cm s}^{-1}$ , an advection speed of  $v_a = 7 \text{ cm s}^{-1}$ , and an advection direction of  $\varphi = 328^\circ$  (i.e. into the cavity). The sense of rotation of the eddy is not necessarily equal to the rotation visualized in the hodograph (Fig. 9a), as  
420 the latter shows the temporal evolution seen by the fixed mooring instrument. Instead, the rotational sense of the eddies can be inferred from a change in the sign of the cross-stream velocity component  $v_n$  relative to the advection direction (Lilly and Rhines, 2002): the sign of  $v_n$  at  $M1_{\text{lower}}$  changes from negative to positive (Fig. 9c), which means that eddies associated with warm events rotate cyclonically (i.e. clockwise in the southern hemisphere). The direct observational link between warm events at depth and eddies advected into the cavity confirms previous model-derived hypotheses of the dynamics of the warm events  
425 (Nøst et al., 2011; Hattermann et al., 2014).

The temperature maximum at  $M1_{\text{lower}}$  occurs by definition at  $t_0$  (Fig. 9a and C1b). The change from negative to positive  $v_n$  also happens at  $t_0$  and does not result from the temperature-based definition of the warm events (Fig. 9c). This change in  $v_n$  indicates that the core of the eddy (Lilly and Rhines, 2002) coincides with the highest temperature, i.e. the highest concentration of dense WDW. The sign of the associated radially inward density gradient is in balance with cyclonic rotation according to  
430 thermal wind balance. This is in agreement with the cyclonic rotation derived from  $v_n$  at  $M1_{\text{lower}}$ . The estimated radius of  $r = 8$  km is in agreement with the magnitude of the baroclinic Rossby radius of  $R = 1\text{-}10$  km in the region. The signature of an eddy in  $v_n$  depends on the properties of the eddy and at which cross-stream radius the eddy passes the mooring (Lilly and Rhines, 2002). The spread in  $v_n$  across the 189 identified events (Fig. 9c) shows that eddies with a variety of properties pass  $M1_{\text{lower}}$  throughout the 12 years. As the variations in  $v_n$  can arise from a combination of changes in the different properties,  
435 we cannot easily quantify the uncertainty in the composite mean eddy properties.

To assess the dynamics below the ice base associated with warm events at depth, Fig. 9b shows a hodograph for  $M1_{\text{upper}}$ , and Fig. 9c shows the corresponding time series of  $v_n$ . Similar to at  $M1_{\text{lower}}$ , the hodograph at  $M1_{\text{upper}}$  rotates anticlockwise around  $t_0$ . In addition, the time series of  $v_n$  (relative to  $\varphi = 328^\circ$ ) agrees well with  $v_n$  at  $M1_{\text{lower}}$ , indicating that the eddies associated with warm events at depth extend up to the ice base. At  $M1_{\text{upper}}$ , the composite temperature and oxygen show  
440 significantly low values before and after  $t_0$ , and the temperature is at a maximum of  $-1.87 \pm 0.08^\circ\text{C}$  at  $t_0$  (Fig. C1b-c).

We also observe a statistically significant temperature maximum of  $-1.77 \pm 0.08^\circ\text{C}$  at  $M2_{\text{lower}}$  six to eight days after  $t_0$  (Fig. C1b). This shows that the WDW advected into the cavity at the main sill via eddies follows, at least to some extent, contours of water column thickness toward the grounding line as proposed by Hattermann et al. (2012) and modeled by Hattermann et al. (2014). The temperature maxima at  $M2_{\text{lower}}$  are not associated with the distinct signature of an eddy like at  $M1$ .

## 445 4 Discussion

### 4.1 Favorable conditions for warm events

We have shown that the highest temperatures at the main sill occur preferably from January to March and from September to November (Fig. 3d and 10b) and that these excursions are associated with eddies advected into the cavity (Fig. 9). In the

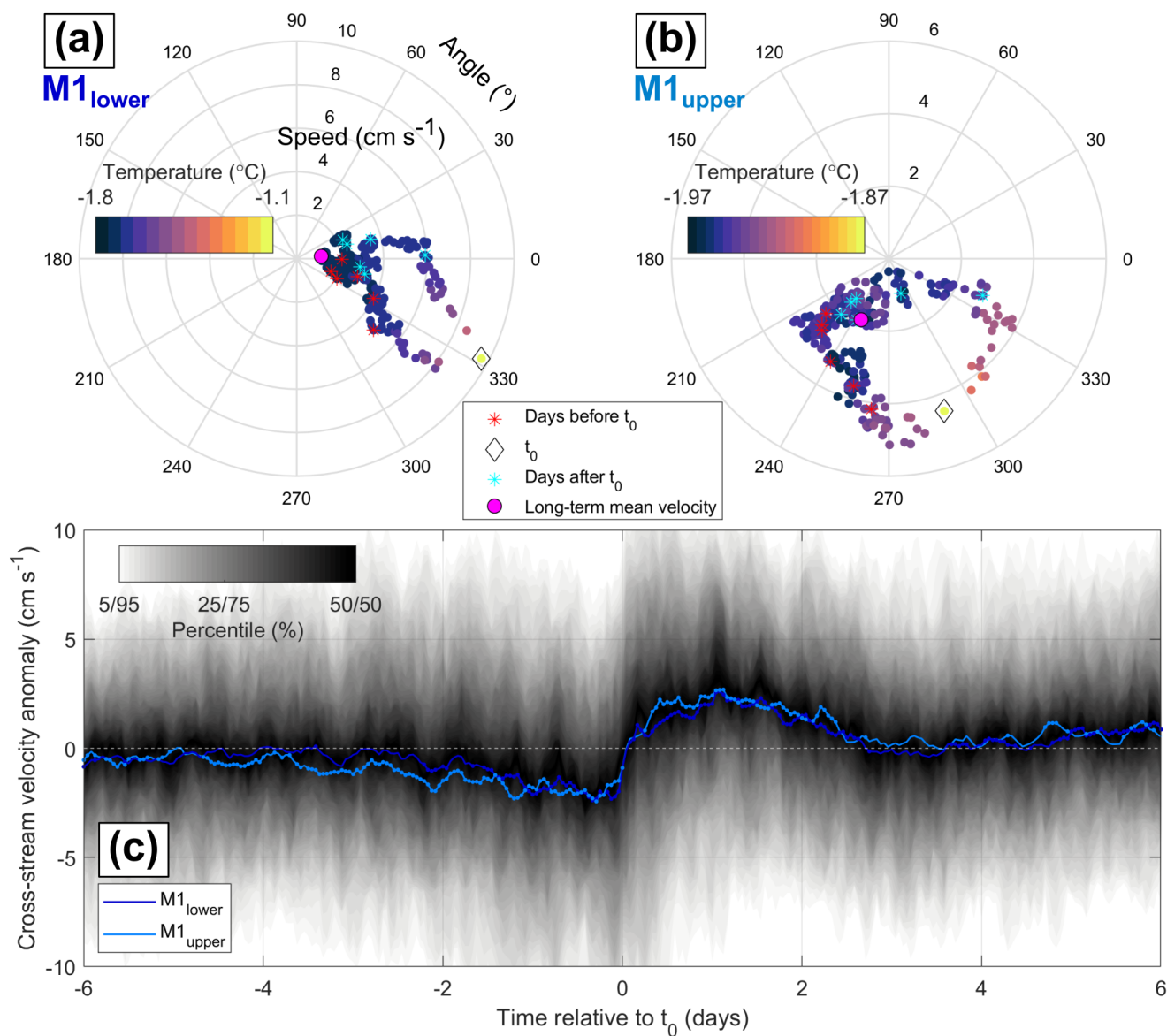


**Figure 9.** Oceanic conditions around warm events at M1<sub>lower</sub> at hourly resolution, as defined in Sect. 2.5. Hodographs (tip of the velocity vector) showing the composite average velocity from six days before to six days after a warm event at  $t_0$  at (a) M1<sub>lower</sub> and (b) M1<sub>upper</sub>. The colormap indicates the respective composite average temperatures at both instruments. Stars indicate the time relative to  $t_0$  on daily resolution. The magenta dot shows the mean velocity during the whole mooring period. Significances for temperature and velocity are shown in Fig. C1b and d, respectively. (c) Composite average cross-stream velocity anomaly (compared to the long-term mean from panels a-b) at M1<sub>lower</sub> and M1<sub>upper</sub> after rotation into the estimated eddy advection direction ( $\varphi = 328^\circ$ ). Dots on the time series indicate a significant deviation from zero (white dashed line). The gray shading shows the percentiles of the velocity distribution at M1<sub>lower</sub> across all 189 events.



following, we discuss potential favorable conditions for warm inflows during these two periods, incorporating also observations  
450 from outside the cavity (Hattermann, 2018; Lauber et al., 2023a).

Modeling studies have suggested that warm intrusions at the main sill occur when the offshore WDW and the associated  
thermocline are lifted over the main sill (Smedsrud et al., 2006; Nicholls et al., 2008; Nøst et al., 2011). Variations of the  
thermocline depth on monthly timescales are driven by the strength of the alongshore winds and freshwater forcing from sea  
ice melt (referred to as external forcing in the following, Lauber et al., 2023a). Downstream at  $17^{\circ}\text{W}$ , the coastal thermocline  
455 is shallowest in February (Fig. 10c, Hattermann, 2018). Upstream at  $10^{\circ}\text{E}$ , observations at  $\text{DML}_{\text{shallow}}$  show the shallowest  
thermocline in March (Fig. 10c), but the minimum in thermocline depth closer to the coast likely occurs earlier than that  
(Lauber et al., 2023a). Therefore, the shallowest externally forced thermocline depth can explain the mWDW/WDW inflow  
that occurs from January to March at  $\text{M1}_{\text{lower}}$  (Fig. 10b), but not the enhanced warm inflow from September to November.

On the upstream and downstream continental shelves, respectively, mooring observations have shown the highest tempera-  
460 tures at depth in January/February at  $39^{\circ}\text{E}$  in front of Shirase Glacier Tongue (Hirano et al., 2020) and in April/May at  $31^{\circ}\text{W}$   
in front of Filchner-Ronne Ice Shelf (Ryan et al., 2017, 2020). This timing of deep warm inflow is consistent with the shal-  
lowest externally forced thermocline above the continental slope in these regions (Ohshima et al., 1996; Semper and Darelius,  
2017). Likewise, at the eastern sill of Fimbulisen, the highest observed temperatures between January and April (Fig. 3f and  
10b) coincide with the shallowest externally forced thermocline (Fig. 10c).

The most obvious difference between the above locations and the main sill of Fimbulisen is the unique geometric configura-  
465 tion of Trolltunga, which overhangs the continental slope. We hypothesize that the seasonal interplay of the ASC with the ice  
shelf plays a role in setting up favorable conditions for WDW intrusions at times other than at the externally forced thermocline  
depth minimum. Recent observational and modeling studies have highlighted the role of conservation of potential vorticity for  
the interaction of the ASC with an ice shelf (Wählin et al., 2020; Steiger et al., 2022). As the ASC follows contours of water  
470 column thickness (Thompson et al., 2018), the presence of Trolltunga may displace the upstream ASC (Fig. 10d) up to 2 km  
northward in front of the main sill (Fig. 10a). This displacement is expected to vary seasonally, as the potential vorticity con-  
straint depends on stratification (Steiger et al., 2022) and baroclinicity (Hattermann et al., 2014, estimated by velocity shear  
at M1, Fig. 10d). Depending on the strength and direction of the ASC in front of the main sill, anomalies in bottom Ekman  
transport may further adjust the depth of the body of WDW on the continental slope (Smedsrud et al., 2006; Webb et al., 2019).  
475 We suggest that this setting of mechanisms provides favorable conditions for the advection of warm eddies across the main sill  
between September and November.

We did not find statistically significant changes in the characteristics of the eddies described in Sect. 3.4 between the two  
seasonal warm inflow periods. Potential mechanisms for the generation of these eddies are (i) the detaching as baroclinic insta-  
bilities from the locally shoaled body of WDW below Trolltunga (Nøst et al., 2011) or (ii) the shedding of barotropic meanders  
480 from the edges of Trolltunga (Walkden et al., 2009). The advection of the eddies across the main sill may be facilitated by a  
mean flow into the cavity from August to February (Fig. 4d). It is unclear if this mean flow causes the warm intrusions and/or  
if it is the result of the seasonal reorganization of water masses inside the cavity (Fig. 7). Although a detailed understanding

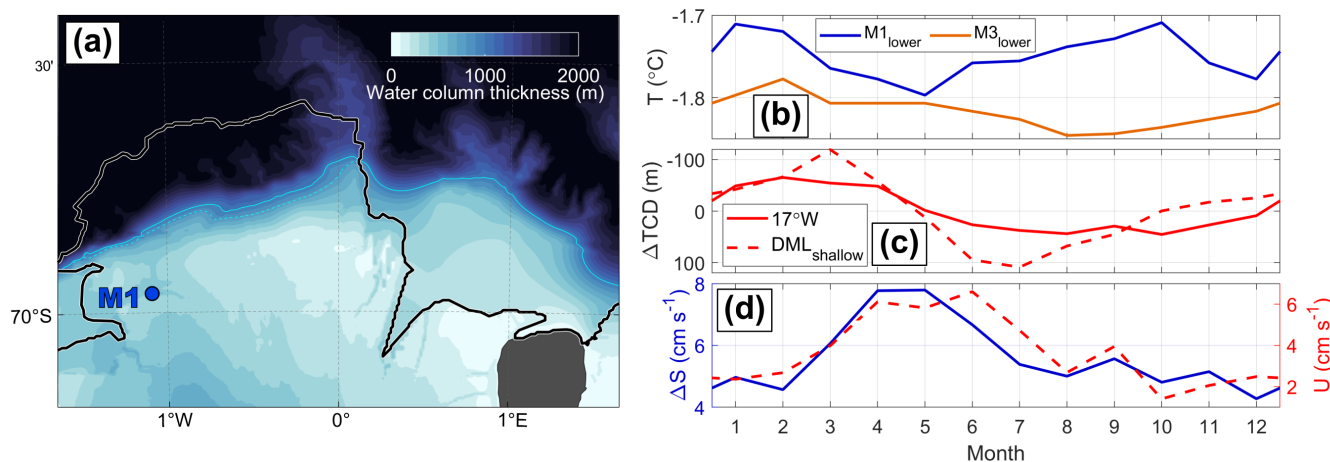


**Figure 10.** (a) Water column thickness at Trolltunga (Morlighem et al., 2020). The black line shows the ice front (Mouginot et al., 2017), the solid cyan line shows the 1000 m water column thickness contour, and the dashed cyan line is the 1000 m isobath (Morlighem et al., 2020). (b) 80 % percentile of the monthly binned temperature distribution at M1<sub>lower</sub> and M3<sub>lower</sub> (middle red lines in Fig. 3d/f). (c) Climatology of monthly thermocline depth anomaly (compared to the respective annual mean) at the coast at 17°W (Hattermann, 2018) and at DML<sub>shallow</sub> (Lauber et al., 2023a). (d) 50 % percentile of the monthly binned velocity shear between M1<sub>upper</sub> and M1<sub>lower</sub> (left axis, lower red line in Fig. 7a), and monthly mean along-stream velocity at the depth of the main sill of 570 m at DML<sub>shallow</sub> (Lauber et al., 2023a).

will require further research, it appears plausible that the interplay of the discussed processes associated with Trolltunga and the externally forced thermocline depth modulates the inflow conditions at the main sill on seasonal timescales.

## 485 4.2 Basal melting

In the following, we discuss the implications of our findings for the basal melting of Fimbulisen. We separate between melting by ASW and by WDW.

### 4.2.1 Melting by ASW

Intrusions of solar-heated ASW below Fimbulisen were observed for the first time by Hattermann et al. (2012) based on the time series from M1<sub>upper</sub> and M3<sub>upper</sub> until January 2012. The authors indicated the possible presence of ASW also at M2<sub>upper</sub>, but did not find robust evidence. Our analyses have extended these results by quantifying the ASW concentrations and taking into account 12 years of temperature and oxygen records. We have shown that the water mass is composed of up to 75 % ASW at 220 m depth in March, and up to 20 % ASW at 370 m depth in June. Derived density gradients have shown that the ASW intrusions are associated with a reorganization of the water masses inside the cavity, separating the colder ISW from the ice base and increasing the thermal forcing there. This demonstrates that ASW can provide heat for basal melting down to ice drafts at 370 m depth, which by far exceeds the depth of 200 m below which Zhou et al. (2014) highlighted the relevance of





ASW for basal melting and the cavity circulation. ~~As such,~~ the contribution of basal melting by ASW below the deep central part of Fimbulisen may be larger than previously thought.

500 ~~At the M2 site,~~ basal melting and its temporal variability has been directly measured by an autonomous phase-sensitive radio-echo sounder (ApRES) deployed between 2017 and 2021 (Lindbäck et al., 2023). The magnitude of the melt rates was inferred to follow the temperature at  $M2_{upper}$  on monthly timescales and the speed of the currents at  $M2_{upper}$  on daily timescales (Lindbäck et al., 2023). This relation was attributed to stronger currents facilitating the turbulent transport of heat toward the ice base. Our observation of ASW at  $M2_{upper}$  complements these results, suggesting that this water mass indeed contributes to delivering heat for basal melting to ~~370 m deep ice.~~

505 We ~~have~~ observed the highest ASW temperatures of up to  $-1.3^{\circ}\text{C}$  in 2016/17 (Fig. 2a/c) when the sea ice concentration in the Weddell Sea and in front of Fimbulisen was at a record low (Turner et al., 2020). Similarly, Lindbäck et al. (2019) found a sudden increase in basal melt rates close to the ice front of Nivlisen Ice Shelf at  $11^{\circ}\text{E}$  during periods when no sea ice was present in front of the ice shelf. These observations are ~~in line~~ with increased solar heating of ASW in the absence of sea ice cover (Kusahara and Hasumi, 2013). In this context, our findings highlight that changes in Southern Ocean heat content (Prince  
510 and L'Ecuyer, 2024) and possibly associated changes in ASW temperature may have direct implications for basal melting ~~down~~  
~~to~~ the deep central part of Fimbulisen.

#### 4.2.2 Melting by WDW

Based on modeling results, Nøst et al. (2011) and Hattermann et al. (2014) have proposed that the transport of mWDW/WDW across the main sill into the Fimbulisen cavity occurs through eddies. Here, we have provided direct observational evidence  
515 for, and additional details on this process: warm events at  $M1_{lower}$  are associated with the signature of eddies, which on average have a radius of 8 km and take about two days ( $= 2\Delta t$ ) to pass the main sill into the cavity. These warm intrusions occur preferably between January and March and between September to November. This finding, together with the potential importance of ASW for melting of deeper ice, can be valuable for interpreting the seasonal variability in satellite-derived basal melt rates (Adusumilli et al., 2020). Traces of WDW at  $M2_{upper}$  confirm that WDW-driven melting of deep ice drives an  
520 overturning circulation (Nøst and Foldvik, 1994) that affects the cavity circulation on seasonal timescales and appears to have strengthened after 2016.

The observed timing of WDW inflows below Fimbulisen suggests that the presence of Trolltunga plays an important role for the inflow dynamics into the cavity. This highlights the potential consequences of the unique setup of the ice shelf and continental slope at Fimbulisen on its mass balance, where future changes in the extent of the ice tongue (~~like the past~~ major  
525 calving event in 1967 (Swithinbank et al., 1977)) may impact the extent to which WDW can access the cavity. However, to ~~more robustly~~ link Trolltunga and associated processes ~~to~~ warm intrusions across the main sill and basal melting of the ice shelf, ~~more work,~~ e.g. using high-resolution numerical modeling, ~~will be needed.~~



## 5 Summary and conclusions

530 The 12 years of temperature, oxygen, and velocity observations below Fimbulisen Ice Shelf have provided new insights into the processes guiding heat into the cavity, both through ASW at the ice base and WDW near the seafloor. Key features identified in the cavity hydrography and circulation are:

- ASW intrudes the cavity below the ice base every year, contributing up to 75 % to the observed water mass composition at 220 m depth in March and up to 20 % at 370 m depth in July.
- 535 – The inflow of ASW along the western side of the Jutulstraumen keel in autumn is in agreement with density gradients derived from velocity shear by thermal wind balance.
- Below a deeper ice draft (350 m), meltwater mixing lines suggest that ISW near the ice base originates from melting by WDW.
- The temperature distribution at the main sill is a superposition of three distinct modes: (i) a background temperature at the surface freezing point, (ii) warm WDW inflow from (a) January to March and (b) September to November, and (iii) 540 cold ISW outflow from May to August.
- Warm events at the main sill are associated with cyclonic eddies that reach up to the ice base.

These results complement the previous mooring studies from Hattermann et al. (2012) and Lauber et al. (2023c) by providing long-term evidence of the temporal and spatial variability of the water masses inside the cavity. The findings highlight the potential future relevance of basal melting of Fimbulisen by ASW and WDW, adding to our understanding of the processes 545 that are important to assess future mass loss of the Antarctic ice sheet and associated sea level rise in a warming climate.

*Code and data availability.* The code to analyze the data and create the figures is available from the corresponding author upon request. The M1-3 mooring data will be updated at <https://doi.org/10.21334/npolar.2023.4a6c36f5> (Lauber et al., 2023b) and made available on full hourly resolution via <https://data.npolar.no>. Winkler titration data and glider data will be made available via <https://data.npolar.no>. The DML mooring data are available at <https://doi.org/10.21334/npolar.2023.45d176be> (Lauber et al., 2024a). The CTD data from the Troll 550 Transect 2020/21 cruise are available at <https://doi.org/10.21334/npolar.2023.b1504a66> (Lauber et al., 2024b). The hydrographic climatology at 17°W is available at <https://doi.org/10.1594/PANGAEA.893199> (Hattermann and Rohardt, 2018). Bathymetric data are available at <https://doi.org/10.1594/PANGAEA.913742> (Eisermann et al., 2020b), <https://doi.org/10.1594/PANGAEA.963737> (Eisermann, 2024), and <https://doi.org/10.1594/PANGAEA.937574> (Dorschel et al., 2022).

### Appendix A: Processing of oxygen data

555 The Oxygen Optodes 3830 mounted on the RCM9s measured the partial pressure of the oxygen dissolved in the seawater through a foil, that is permeable to gas, but not water or salt. The large amount of noise toward low values in the oxygen



records from the optodes requires careful processing of these data. No noise is present toward higher oxygen values, making high values generally more reliable than low values. The steps undertaken to process the data are summarized below:

1. Salinity and pressure correction:

560 The raw data from the instruments were corrected for the effects of salinity and pressure. This was done following the procedure recommended by the manufacturer (Aanderaa Data Instruments, 2007):

$$DO_{corr} = DO_{uncorr} f_S f_P, \quad (A1)$$

where  $DO_{corr}$  is the corrected oxygen,  $DO_{uncorr}$  is the uncorrected oxygen, and  $f_S$  and  $f_P$  are factors compensating the effects of salinity and pressure, respectively. These factors are given by

565 
$$f_S = \exp((S - S_{int})(B_0 + B_1 T_S + B_2 T_S^2 + B_3 T_S^3) + C_0(S^2 - S_{int}^2)) \quad (A2)$$

$$f_P = 1 + \frac{0.032D}{1000\text{m}}, \quad (A3)$$

570 where  $S$  is the practical salinity measured by the RCM9,  $S_{int} = 1$  psu is a fixed internal salinity setting of the optode,  $T_S$  is the scaled temperature (defined below),  $B_{0...3}$  and  $C_0$  are constants (given in Table A1), and  $D$  is the depth of the sensor. As salinity measurements were only available until the end of 2010,  $S$  was set to the time-mean of each instrument over this period. An increase in  $S$  by 0.1 psu leads to a decrease in  $DO_{corr}$  by  $0.005 \text{ ml l}^{-1}$  at the typically measured salinities, i.e. the sensitivity of  $DO_{corr}$  to temporal changes in salinity is negligible. At  $M3_{upper}$ , where no salinity measurements were available,  $S$  was set to the mean salinity of  $M1_{upper}$ . The scaled temperature  $T_S$  is given by

$$T_S = \ln\left(\frac{298.15^\circ\text{C} - T}{273.15^\circ\text{C} + T}\right), \quad (A4)$$

where  $T$  is the in situ temperature in  $^\circ\text{C}$  measured by the RCM9.

575 2. Unit conversion:

The unit given by the instrument is  $\mu\text{mol l}^{-1}$ . This unit was converted into  $\text{ml l}^{-1}$ :

$$\frac{\text{ml}}{\text{l}} = 10^{-3} \frac{\mu\text{mol}}{\text{l}} V, \quad (A5)$$

where  $V = 22.41 \text{ l mol}^{-1}$  is the molar volume of an ideal gas at standard temperature and pressure.

3. Offset removal:

580 We identified an offset of  $0.4 \text{ ml l}^{-1}$  in the sub-ice-shelf oxygen data compared to the auxiliary data sets. At the lower instruments, this offset was obtained from the difference between the respective WDW-WW mixing lines in the  $\Theta$ - $DO$  diagram (Fig. 5). This mixing line is most pronounced at  $M1_{lower}$  (due to the strongest WDW influence), but is also present to some extent at  $M2_{lower}$  and  $M3_{lower}$ . Therefore, to remove the offset, we added a constant value of  $0.4 \text{ ml l}^{-1}$  to the oxygen data of all lower instruments.



585 At the upper instruments, an offset is ~~harder~~ to identify than at the lower instruments in the  $\Theta$ -DO diagram (Fig. 5), as the water masses do not follow a clear mixing line. A mixing line between ASW and WW is more pronounced in the Winkler titration data in a  $S_A$ -DO diagram (Fig. A1, based only on data until the end of 2010). The slope of the ASW-WW mixing line at  $M1_{\text{upper}}$  agrees with the slope of the line from the Winkler titration data, yielding the same offset of  $0.4 \text{ ml l}^{-1}$  as for the lower instruments. For  $M2_{\text{upper}}$ , the  $S_A$ -DO diagram is less conclusive since most of the  
 590 observed water is ISW, ~~but this~~ is not represented in the auxiliary data. However, after adding the same offset to the  $M2_{\text{upper}}$  oxygen data, the  $S_A$ -DO properties can be traced back along a meltwater mixing line to originate from WW in all three auxiliary data sets (Fig. A1). At  $M3_{\text{upper}}$  no comparison in  $S_A$ -DO space can be done due to missing salinity data. However, ~~due to~~ similar temperature values (Fig. 2a/c) and a similar seasonal variability in temperature (Fig. 3a/c) and oxygen (Fig. A2) at  $M3_{\text{upper}}$  compared to  $M1_{\text{upper}}$ , and because the magnitude of the oxygen offset was the same  
 595 at all ~~other~~ five instruments, the constant of  $0.4 \text{ ml l}^{-1}$  was also added to the oxygen records at  $M3_{\text{upper}}$ .

The coefficients to convert the raw instrument voltage from the instrument into engineering units of dissolved oxygen are the same for all six optodes. This may explain why the offset in absolute oxygen values is also the same. However, after consulting the instrument manufacturer, we cannot ~~conclude on~~ the origin of this offset.

#### 4. Noise removal:

600 This step was done separately for the upper and lower sensors, due to different temperature-oxygen properties below the ice base compared ~~to~~ close to the seabed.

(a) For the upper oxygen sensors, all values below a threshold of  $6.5 \text{ ml l}^{-1}$  were discarded. After that, the hourly data were subsampled by selecting the maximum hourly measurement for each day. If one or more measurements during one day had already been discarded, no measurement was kept for the respective day. This method yields  
 605 the upper envelope of the oxygen time series and strictly removes any suspicious spikes toward low values.

(b) For all lower oxygen sensors, low oxygen values accompanied by an increase in temperature were identified as real features in Fig. 5, as they lay on the WW-WDW mixing line. Using the same method as for the upper sensors would remove these values. To avoid this, we define a threshold based on both oxygen and temperature, below which all data oxygen measurements were removed. This threshold is set directly below the WW-WDW mixing  
 610 line (black-white dashed line in Fig. 5), and is described by the equation

$$DO = 5 \text{ ml l}^{-1} - 1 \text{ ml l}^{-1} \text{ } ^\circ\text{C}^{-1} \Theta. \quad (\text{A6})$$

To account for any remaining artifacts in the absolute values of dissolved oxygen, we used an uncertainty of  $\sigma_{DO} = 0.1 \text{ ml l}^{-1}$  in the OMP calculations (see Appendix B).



**Table A1.** Constants used for the compensation of salinity at the Oxygen Optodes 3830.

$B_0$	$-6.24097 \times 10^{-3} \text{ psu}^{-1}$
$B_1$	$-6.93498 \times 10^{-3} \text{ psu}^{-1} \text{ }^\circ\text{C}^{-1}$
$B_2$	$-6.90358 \times 10^{-3} \text{ psu}^{-1} \text{ }^\circ\text{C}^{-2}$
$B_3$	$-4.29155 \times 10^{-3} \text{ psu}^{-1} \text{ }^\circ\text{C}^{-3}$
$C_0$	$-3.11680 \times 10^{-7} \text{ psu}^{-2}$

### Appendix B: Uncertainty analysis of the OMP analysis

615 The uncertainties of the water mass fractions  $x$  from the OMP analysis were calculated using a Monte Carlo approach: First, uncertainties were assigned to the tracer properties of the source water masses (Table 2, Fig. B1) and the measured tracers ( $\sigma_\Theta = 0.05 \text{ }^\circ\text{C}$ ,  $\sigma_{S_A} = 0.05 \text{ g kg}^{-1}$ ,  $\sigma_{DO} = 0.1 \text{ ml l}^{-1}$ ). Then, the OMP calculation for the mean and the daily averages was re-run  $10^5$  times, but with all source water properties and measured values perturbed by a randomly drawn value of a normal distribution with zero mean and the respective uncertainty of the tracers as standard deviation. The standard deviation of the  
620 distribution from all perturbed runs was then taken as the error of the water mass fractions.

### Appendix C: Significance and uncertainty analysis for warm events

The statistical significance of the time series before and after the warm events was calculated using a Monte Carlo approach: for each variable at each instrument, the number of events, over which the value at the respective lag was averaged (referred to as original average in the following), was stored. This number varies due to gaps in some of the time series. It was then tested  
625  $10^5$  times how often the original average is greater or lower than an average based on the same number of events, but from values randomly drawn from the respective full time series. If for at least 99 % of the tests the original average was larger, or for at least 99 % of the tests the original average was smaller than the random average, the value was considered significant.

The uncertainty of the composite averages was assessed by taking the standard deviation of all included variables across all events on hourly resolution before, after, and during an event.

630 *Author contributions.* JL processed the data, conducted the analyses, prepared the figures, and wrote the first version of the manuscript. TH participated in the fieldwork and provided supervision. JL, TH, LdS, and ED discussed and improved the manuscript.

*Competing interests.* The authors declare that they have no conflict of interest.

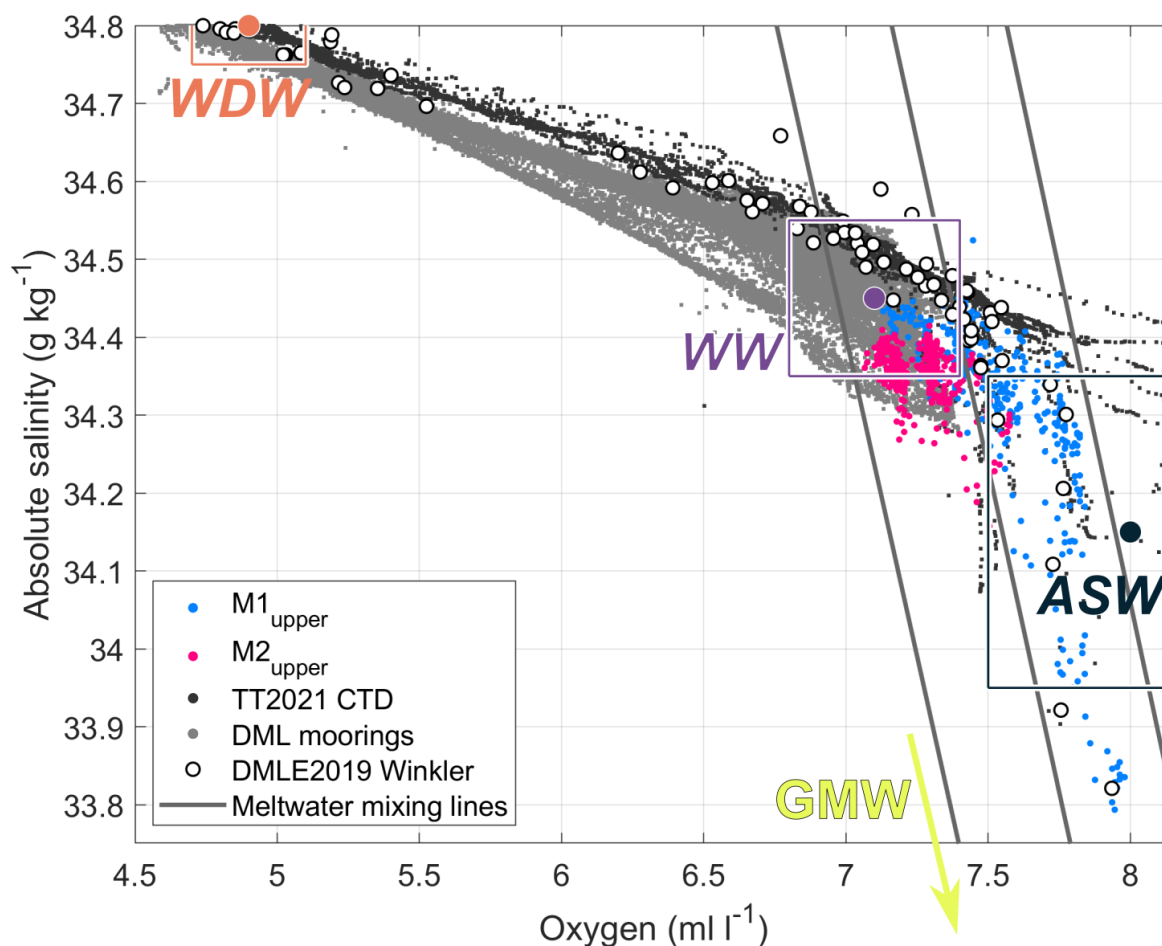


**Figure A1.** Absolute salinity - dissolved oxygen diagram of  $M1_{upper}$  and  $M2_{upper}$  after removal of the constant offset and noise until the end of 2010 (since no salinity data are available afterward). The same auxiliary data sets as in Fig. 5, Fig. B1, and Fig. B2 are shown. Colored dots with boxes indicate the mean properties and uncertainties of ASW, WW, and WDW (see also Table 2).

*Acknowledgements.* This research was funded by the Research Council of Norway through the KLIMAFORSK program (project iMelt, 295075). The installation of the moorings through the project ‘ICE Fimbulisen - top to bottom’ in 2009 was financed by the Centre for Ice, Climate and Ecosystems (ICE), Norwegian Polar Institute (NPI). The moorings were maintained by NPI through ICE, the Norwegian Antarctic Research Expedition (IceRises 759, 3801-103) and iMelt. The DML moorings were financed and installed by NPI. J.L. was funded by iMelt, and T.H. by the European Union’s Horizon 2020 program (CRiceS, 101003826). The authors thank the sections Maritime and Technical Support and Operations and Logistics Antarctica from NPI for their support involving the moorings. The authors also thank Morven Muilwijk for helpful discussions on the Optimum Multiparameter analysis.

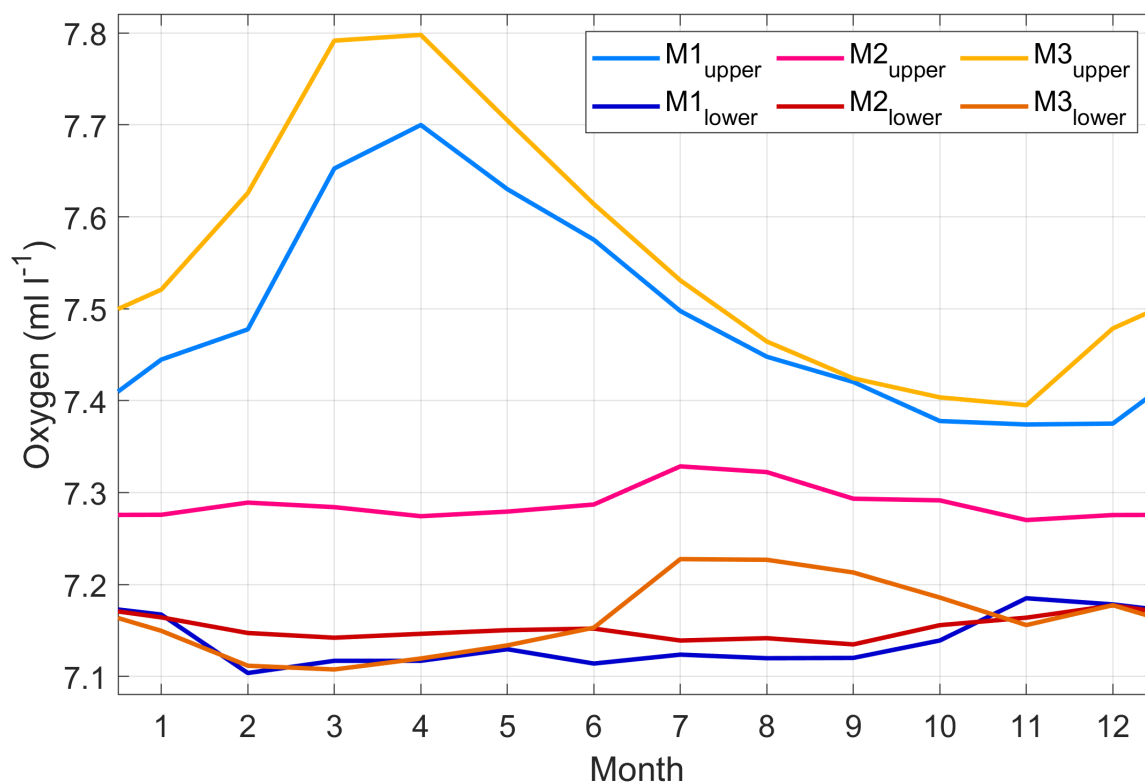


**Figure A2.** Monthly averaged climatology of dissolved oxygen (after offset and noise removal) at all sub-ice-shelf mooring instruments.

## 640 References

- Aanderaa Data Instruments: TD 218 Operating Manual Oxygen Optode 3830, 3835, 3930, 3975, 4130, 4175, Bergen, Norway, 2007.
- Adusumilli, S., Fricker, H. A., Medley, B., Padman, L., and Siegfried, M. R.: Interannual variations in meltwater input to the Southern Ocean from Antarctic ice shelves, *Nature Geoscience*, 13, 616–620, 2020.
- Alken, P., Thébaud, E., Beggan, C. D., Amit, H., Aubert, J., Baerenzung, J., Bondar, T., Brown, W., Califf, S., Chambodut, A., Chulliat, A., Cox, G. A., Finlay, C. C., Fournier, A., Gillet, N., Grayver, A., Hammer, M. D., Holschneider, M., Huder, L., Hulot, G., Jager, T., Kloss, C., Korte, M., Kuang, W., Kuvshinov, A., Langlais, B., Léger, J.-M., Lesur, V., Livermore, P. W., Lowes, F. J., Macmillan, S., Magnes, W., Manda, M., Marsal, S., Matzka, J., Metman, M. C., Minami, T., Morschhauser, A., Mound, J. E., Nair, M., Nakano, S., Olsen, N., Pavón-Carrasco, F. J., Petrov, V. G., Ropp, G., Rother, M., Sabaka, T. J., Sanchez, S., Saturnino, D., Schnepf, N. R., Shen, X., Stolle, C., Tangborn, A., Tøffner-Clausen, L., Toh, H., Torta, J. M., Varner, J., Vervelidou, F., Vigneron, P., Wardinski, I., Wicht, J., Woods, A., Yang, Y., Zeren, Z., and Zhou, B.: International Geomagnetic Reference Field: the thirteenth generation, *Earth, Planets and Space*, 73, 1–25, <https://doi.org/10.1186/s40623-020-01288-x>, 2021.
- Biddle, L. C., Heywood, K. J., Kaiser, J., and Jenkins, A.: Glacial Meltwater Identification in the Amundsen Sea, *Journal of Physical Oceanography*, 47, 933 – 954, <https://doi.org/10.1175/JPO-D-16-0221.1>, 2017.

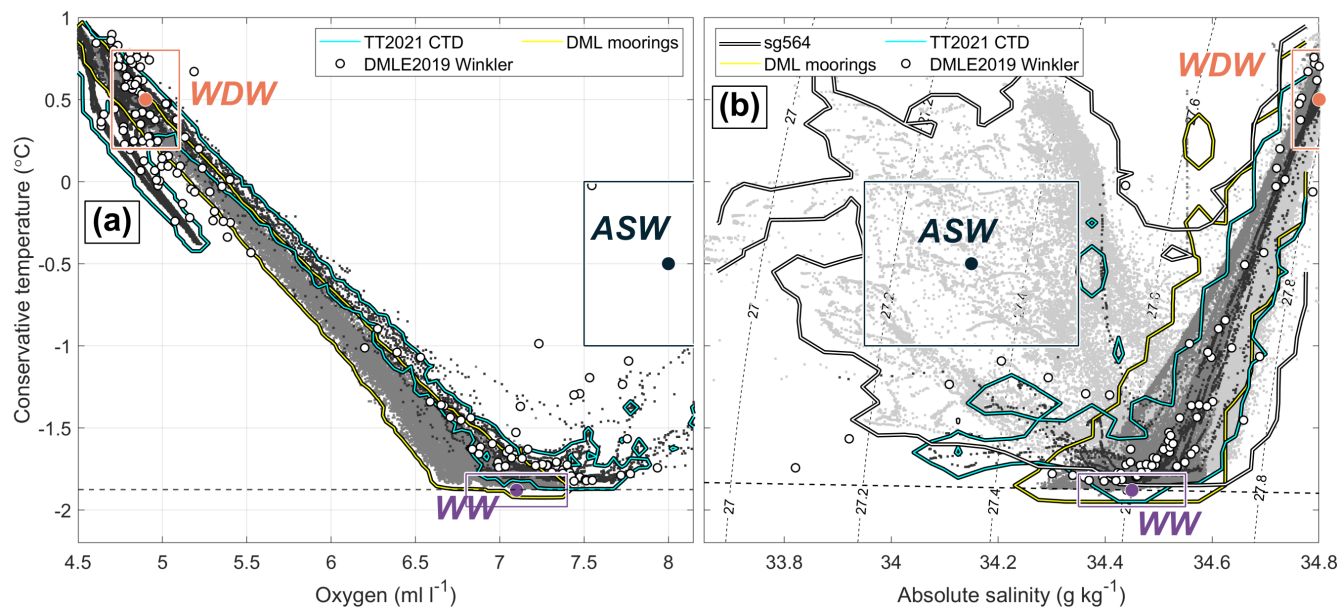


**Figure B1.** Mean properties and uncertainties of the source water masses (except Glacial Meltwater). (a) Conservative temperature - dissolved oxygen diagram and (b) conservative temperature - absolute salinity diagram. The same auxiliary data sets as in Fig. 5 and Fig. B2 are shown, with all data points indicated in gray tones. Colored dots with boxes indicate the mean properties and uncertainties of ASW, WW, and WDW (see also Table 2).

Chelton, D. B., deSzoeko, R. A., Schlax, M. G., Naggar, K. E., and Siwertz, N.: Geographical Variability of the First  
 655 Baroclinic Rossby Radius of Deformation, *Journal of Physical Oceanography*, 28, 433–460, [https://doi.org/10.1175/1520-0485\(1998\)028<0433:GVOTFB>2.0.CO;2](https://doi.org/10.1175/1520-0485(1998)028<0433:GVOTFB>2.0.CO;2), 1998.

DeConato, R. M. and Pollard, D.: Contribution of Antarctica to past and future sea-level rise, *Nature*, 531, 591–597, 2016.

DeConato, R. M., Pollard, D., Alley, R. B., Velicogna, I., Gasson, E., Gomez, N., Sadai, S., Condron, A., Gilford, D. M., Ashe, E. L., Kopp, R. E., Li, D., and Dutton, A.: The Paris Climate Agreement and future sea-level rise from Antarctica, *Nature*, 593, 83–89, 2021.

660 Dorschel, B., Hehemann, L., Viquerat, S., Warnke, F., Dreutter, S., Schulze Tenberge, Y., Accettella, D., An, L., Barrios, F., Bazhenova, E. A., Black, J., Bohoyo, F., Davey, C., de Santis, L., Escutia Dotti, C., Fremand, A. C., Fretwell, P. T., Gales, J. A., Gao, J., Gasperini, L., Greenbaum, J. S., Henderson Jencks, J., Hogan, K. A., Hong, J. K., Jakobsson, M., Jensen, L., Kool, J., Larin, S., Larter, R. D., Leitchenkov, G. L., Loubrieu, B., Mackay, K., Mayer, L., Millan, R., Morlighem, M., Navidad, F., Nitsche, F.-O., Nogi, Y., Pertuisot, C., Post, A. L., Pritchard, H. D., Purser, A., Rebesco, M., Rignot, E., Roberts, J. L., Rovere, M., Ryzhov, I., Sauli, C., Schmitt, T., Silvano,  
 665 A., Smith, J. E., Snaith, H., Tate, A. J., Tinto, K., Vandenbossche, P., Weatherall, P., Wintersteller, P., Yang, C., Zhang, T., and Arndt, J. E.: The International Bathymetric Chart of the Southern Ocean Version 2 (IBCSO v2), PANGAEA, URL: <https://doi.org/10.1594/PANGAEA.937574>. Last accessed: 15.06.2022, 2022.

Dorschel, B., Hehemann, L., Viquerat, S., Warnke, F., Dreutter, S., Tenberge, Y. S., Accettella, D., An, L., Barrios, F., Bazhenova, E., et al.: The International Bathymetric Chart of the Southern Ocean Version 2, *Scientific Data*, 9, 1–13, 2022.



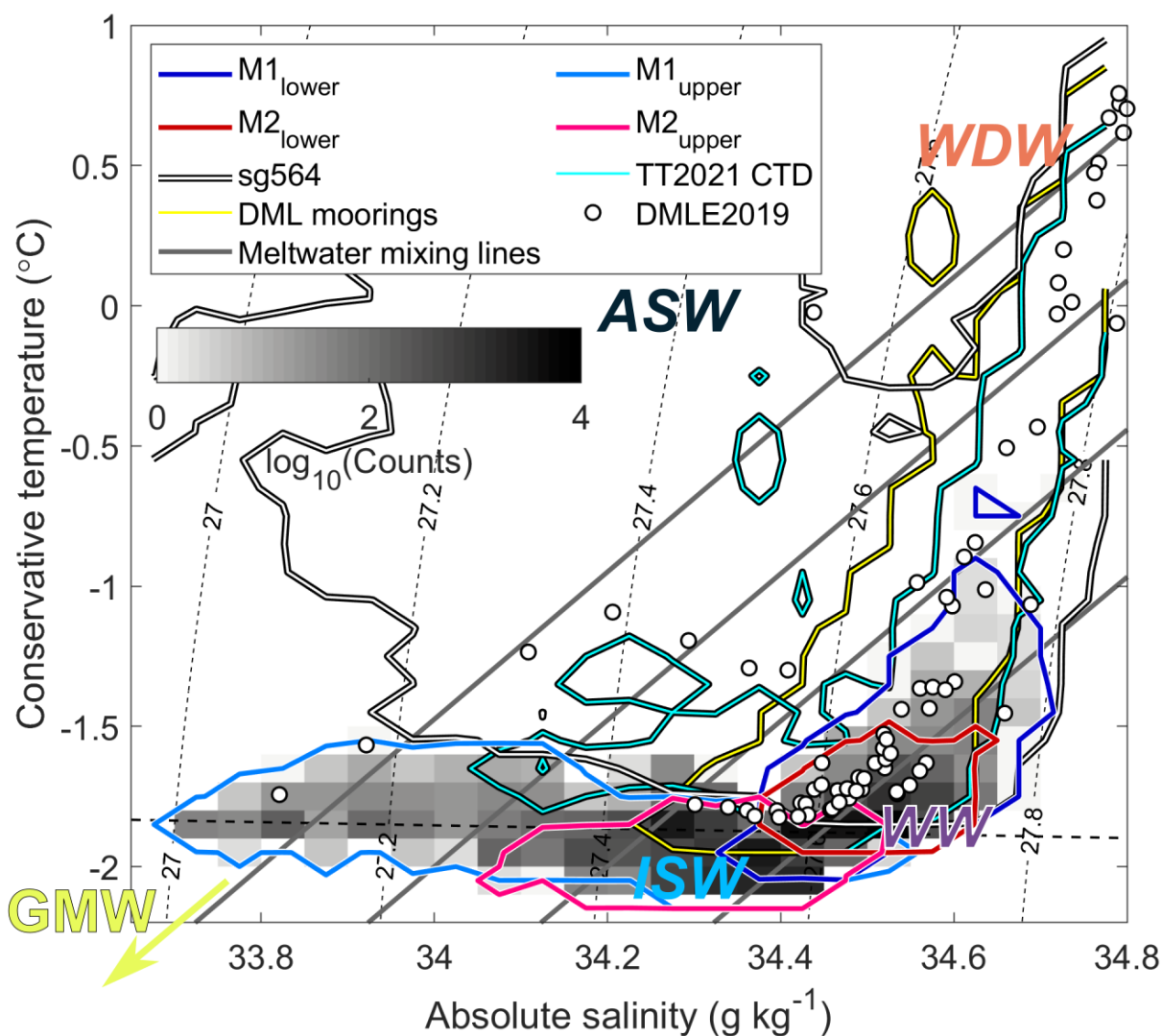


**Figure B2.** Conservative temperature - absolute salinity diagram of the sub-ice-shelf mooring data and auxiliary data. The gray shading is a histogram of all hourly upper and lower mooring data until the end of 2010.  $M3_{upper}$  and  $M3_{lower}$  are not included in this figure due to missing or unreliable conductivity data. Colored lines show the range of the single mooring instruments (blue, red, 1 count contour), of the  $DML_{deep}/DML_{shallow}$  mooring data (yellow, 5 counts contour), of the Troll Transect 2020/21 CTD data (cyan, 5 counts contour), and a glider (sg564, white, 5 counts contour). White dots are data from CTD stations during the Southern Ocean Ecosystem cruise 2019. The shown data points are the same as for the Winkler titration data in Fig. 5. The gray lines are meltwater mixing lines. The near-horizontal black dashed line indicates the salinity-dependent surface freezing point. Dashed contours indicate the potential density in  $kg\ m^{-3}$ .

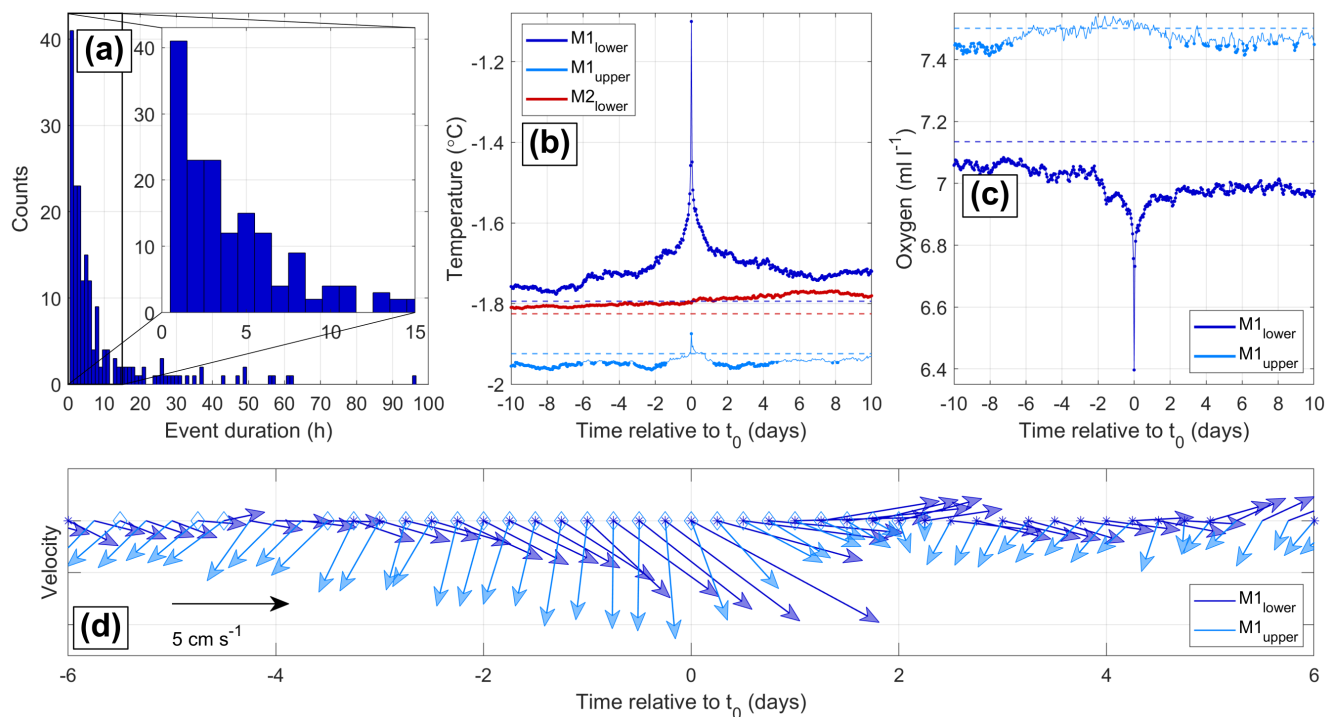


**Figure C1.** Additional statistics of warm events at  $M1_{lower}$ . (a) Histogram of the event duration. Composite averages of temperature (b) and dissolved oxygen (c) before, during, and after an event. Dots on the time series indicate a significant deviation from the long-term mean (dashed lines). (d) Composite averages of velocity at  $M1_{upper}$  and  $M1_{lower}$  before, during, and after an event. For clarity, arrows are plotted every six hours. Significant values are marked at  $M1_{lower}$  with a star and at  $M1_{upper}$  with a diamond.

- 670 Dupont, T. K. and Alley, R. B.: Assessment of the importance of ice-shelf buttressing to ice-sheet flow, *Geophysical Research Letters*, 32, L04 503, <https://doi.org/10.1029/2004GL022024>, 2005.
- Dutrieux, P., Rydt, J. D., Jenkins, A., Holland, P. R., Ha, H. K., Lee, S. H., Steig, E. J., Ding, Q., Abrahamsen, E. P., and Schröder, M.: Strong Sensitivity of Pine Island Ice-Shelf Melting to Climatic Variability, *Science*, 343, 174–178, <https://doi.org/10.1126/science.1244341>, 2014.
- 675 Edwards, T. L., Nowicki, S., Marzeion, B., Hock, R., Goelzer, H., Seroussi, H., Jourdain, N. C., Slater, D. A., Turner, F. E., Smith, C. J., et al.: Projected land ice contributions to twenty-first-century sea level rise, *Nature*, 593, 74–82, 2021.
- Eisermann, H.: Bathymetric model beneath Nivl and Lazarev ice shelves, and across Astrid Ridge embedded within IBCSOV2, PANGAEA, URL: <https://doi.org/10.1594/PANGAEA.963737>. Last accessed: 05.03.2024, 2024.
- Eisermann, H., Eagles, G., Ruppel, A., Smith, E. C., and Jokat, W.: Bathymetry Beneath Ice Shelves of Western Dronning Maud Land, East Antarctica, and Implications on Ice Shelf Stability, *Geophysical Research Letters*, 47, 1–10, 2020a.
- 680 Eisermann, H., Eagles, G., Ruppel, A., Smith, E. C., and Jokat, W.: Bathymetry beneath ice shelves of western Dronning Maud Land, East Antarctica, PANGAEA, URL: <https://doi.org/10.1594/PANGAEA.913742>. Last accessed: 30.03.2022, 2020b.
- Eisermann, H., Eagles, G., and Jokat, W.: Coastal bathymetry in central Dronning Maud Land controls ice shelf stability, *Scientific Reports*, 14, 1–13, <https://doi.org/10.1038/s41598-024-51882-2>, 2024.



- Foldvik, A., Gammelsrød, T., Østerhus, S., Fahrbach, E., Rohardt, G., Schröder, M., Nicholls, K. W., Padman, L., and Woodgate, R. A.: Ice shelf water overflow and bottom water formation in the southern Weddell Sea, *Journal of Geophysical Research: Oceans*, 109, 1–15, 2004.
- 685 Gade, H. G.: Melting of Ice in Sea Water: A Primitive Model with Application to the Antarctic Ice Shelf and Icebergs, *Journal of Physical Oceanography*, 9, 189 – 198, [https://doi.org/10.1175/1520-0485\(1979\)009<0189:MOIISW>2.0.CO;2](https://doi.org/10.1175/1520-0485(1979)009<0189:MOIISW>2.0.CO;2), 1979.
- Greene, C. A., Gwyther, D. E., and Blankenship, D. D.: Antarctic Mapping Tools for Matlab, *Computers & Geosciences*, 104, 151–157, <https://doi.org/10.1016/j.cageo.2016.08.003>, 2017.
- 690 Greene, C. A., Gardner, A. S., Schlegel, N.-J., and Fraser, A. D.: Antarctic calving loss rivals ice-shelf thinning, *Nature*, 609, 948–953, 2022.
- Hattermann, T.: Antarctic Thermocline Dynamics along a Narrow Shelf with Easterly Winds, *Journal of Physical Oceanography*, 48, 2419–2443, 2018.
- Hattermann, T. and Rohardt, G.: Kapp Norvegia Antarctic Slope Front climatology, Alfred Wegener Institute, Helmholtz Centre for Polar and Marine Research, Bremerhaven, PANGAEA, URL: <https://doi.org/10.1594/PANGAEA.893199>. Last accessed: 24.08.2022, 2018.
- 695 Hattermann, T., Nøst, O. A., Lilly, J. M., and Smedsrud, L. H.: Two years of oceanic observations below the Fimbul Ice Shelf, *Antarctica, Geophysical Research Letters*, 39, 1–6, 2012.
- Hattermann, T., Smedsrud, L. H., Nøst, O. A., Lilly, J. M., and Galton-Fenzi, B. K.: Eddy-resolving simulations of the Fimbul Ice Shelf cavity circulation: Basal melting and exchange with open ocean, *Ocean Modelling*, 82, 28–44, 2014.
- Hellmer, H. H., Jacobs, S. S., and Jenkins, A.: Ocean, Ice, and Atmosphere: Interactions at the Antarctic Continental Margin, chap. Oceanic Erosion of a Floating Antarctic Glacier in the Amundsen Sea, pp. 83–99, American Geophysical Union (AGU), <https://doi.org/10.1029/AR075p0083>, 1998.
- 700 Herraiz-Borreguero, L. and Naveira Garabato, A. C.: Poleward shift of Circumpolar Deep Water threatens the East Antarctic Ice Sheet, *Nature Climate Change*, 12, 728–734, 2022.
- Hirano, D., Tamura, T., Kusahara, K., Ohshima, K. I., Nicholls, K. W., Ushio, S., Simizu, D., Ono, K., Fujii, M., Nogi, Y., and Aoki, S.: Strong ice-ocean interaction beneath Shirase Glacier Tongue in East Antarctica, *Nature Communications*, 11, 1–12, 2020.
- 705 Jacobs, S. S.: On the nature and significance of the Antarctic Slope Front, *Marine Chemistry*, 35, 9–24, [https://doi.org/10.1016/S0304-4203\(09\)90005-6](https://doi.org/10.1016/S0304-4203(09)90005-6), 1991.
- Jenkins, A.: The Impact of Melting Ice on Ocean Waters, *Journal of Physical Oceanography*, 29, 2370 – 2381, [https://doi.org/10.1175/1520-0485\(1999\)029<2370:TIOMIO>2.0.CO;2](https://doi.org/10.1175/1520-0485(1999)029<2370:TIOMIO>2.0.CO;2), 1999.
- 710 Jenkins, A. and Jacobs, S.: Circulation and melting beneath George VI Ice Shelf, *Antarctica, Journal of Geophysical Research: Oceans*, 113, <https://doi.org/10.1029/2007JC004449>, 2008.
- Jenkins, A., Shoosmith, D., Dutrieux, P., Jacobs, S., Kim, T. W., Lee, S. H., Ha, H. K., and Stammerjohn, S.: West Antarctic Ice Sheet retreat in the Amundsen Sea driven by decadal oceanic variability, *Nature Geoscience*, 11, 733–738, 2018.
- Kusahara, K. and Hasumi, H.: Modeling Antarctic ice shelf responses to future climate changes and impacts on the ocean, *Journal of Geophysical Research: Oceans*, 118, 2454–2475, <https://doi.org/10.1002/jgrc.20166>, 2013.
- 715 Lauber, J., de Steur, L., Hattermann, T., and Darelus, E.: Observed Seasonal Evolution of the Antarctic Slope Current System off the Coast of Dronning Maud Land, East Antarctica, ESS Open Archive, <https://doi.org/10.22541/essoar.169755155.52018682/v1>, 2023a.
- Lauber, J., de Steur, L., Hattermann, T., and Nøst, O. A.: Daily averages of physical oceanography and current meter data from sub-ice-shelf moorings M1, M2 and M3 at Fimbulisen, East Antarctica since 2009, Norwegian Polar Institute, Tromsø, <https://doi.org/10.21334/npolar.2023.4a6c36f5>, 2023b.
- 720



- Lauber, J., Hattermann, T., de Steur, L., Darelius, E., Auger, M., Nøst, O., and Moholdt, G.: Warming beneath an East Antarctic ice shelf due to increased subpolar westerlies and reduced sea ice, *Nature Geoscience*, <https://doi.org/10.1038/s41561-023-01273-5>, 2023c.
- Lauber, J., de Steur, L., Hattermann, T., and Lundesgaard, Ø.: Hydrography and current meter data from two ocean moorings off the coast of Dronning Maud Land 2019–2021, Norwegian Polar Institute, Tromsø, <https://doi.org/10.21334/npolar.2023.45d176be>, 2024a.
- 725 Lauber, J., Hattermann, T., Moreau, S., Dundas, V., and Lundesgaard, Ø.: CTD profiles from Troll Transect cruise 2020–2021 to Dronning Maud Land, Antarctica, Norwegian Polar Institute, Tromsø, <https://doi.org/10.21334/npolar.2023.b1504a66>, 2024b.
- Lawson, C. L. and Hanson, R. J.: Solving Least Squares Problems, chap. Linear Least Squares with Linear Inequality Constraints, pp. 158–173, Prentice Hall, Hoboken, New Jersey, <https://doi.org/10.1137/1.9781611971217.ch23>, 1974.
- Lilly, J. M.: jLab: A data analysis package for Matlab, v.1.7.1, [Computer software], <https://doi.org/10.5281/zenodo.4547006>, 2021.
- 730 Lilly, J. M. and Rhines, P. B.: Coherent Eddies in the Labrador Sea Observed from a Mooring, *Journal of Physical Oceanography*, 32, 585–598, [https://doi.org/10.1175/1520-0485\(2002\)032<0585:CEITLS>2.0.CO;2](https://doi.org/10.1175/1520-0485(2002)032<0585:CEITLS>2.0.CO;2), 2002.
- Lindbäck, K., Moholdt, G., Nicholls, K. W., Hattermann, T., Pratap, B., Thamban, M., and Matsuoka, K.: Spatial and temporal variations in basal melting at Nivlisen ice shelf, East Antarctica, derived from phase-sensitive radars, *The Cryosphere*, 13, 2579–2595, 2019.
- Lindbäck, K., Darelius, E., Moholdt, G., Vaňková, I., Hattermann, T., Lauber, J., and de Steur, L.: Basal melting and oceanic observations  
735 beneath Fimbulisen, East Antarctica, Preprint available at ESS Open Archive, <https://doi.org/10.22541/essoar.170365303.33631810/v1>, 2023.
- Mackas, D. L., Denman, K. L., and Bennett, A. F.: Least squares multiple tracer analysis of water mass composition, *Journal of Geophysical Research: Oceans*, 92, 2907–2918, <https://doi.org/10.1029/JC092iC03p02907>, 1987.
- McDougall, T. J. and Barker, P. M.: Getting started with TEOS-10 and the Gibbs Seawater (GSW) Oceanographic Toolbox, *Scor/Iapso*  
740 *WG127*, pp. 1–32, 2011.
- McPhee, M. and Morison, J.: Under-ice boundary layer, *Encyclopedia of Ocean Sciences*, pp. 3071–3078, <https://doi.org/10.1006/rwos.2001.0146>, 2001.
- Morlighem, M., Rignot, E., Binder, T., Blankenship, D., Drews, R., Eagles, G., Eisen, O., Ferraccioli, F., Forsberg, R., Fretwell, P., et al.: Deep glacial troughs and stabilizing ridges unveiled beneath the margins of the Antarctic ice sheet, *Nature Geoscience*, 13, 132–137, 2020.
- 745 Mouginot, J., Scheuchl, B., and Rignot, E.: MEaSUREs Antarctic Boundaries for IPY 2007–2009 from Satellite Radar, Version 2. [Coastline\_Antarctica\_v02, GroundingLine\_Antarctica\_v02], NASA National Snow and Ice Data Center Distributed Active Archive Center. Boulder/Colorado/USA., URL: <https://nsidc.org/data/NSIDC-0709>. Last accessed: 30.07.2021, 2017.
- Nakayama, Y., Schröder, M., and Hellmer, H.: From circumpolar deep water to the glacial meltwater plume on the eastern Amundsen Shelf, *Deep Sea Research Part I: Oceanographic Research Papers*, 77, 50–62, <https://doi.org/10.1016/j.dsr.2013.04.001>, 2013.
- 750 Nicholls, K. W., Abrahamsen, E. P., Buck, J. J. H., Dodd, P. A., Goldblatt, C., Griffiths, G., Heywood, K. J., Hughes, N. E., Kaletsky, A., Lane-Serff, G. F., McPhail, S. D., Millard, N. W., Oliver, K. I. C., Perrett, J., Price, M. R., Pudsey, C. J., Saw, K., Stansfield, K., Stott, M. J., Wadhams, P., Webb, A. T., and Wilkinson, J. P.: Measurements beneath an Antarctic ice shelf using an autonomous underwater vehicle, *Geophysical Research Letters*, 33, 1–4, <https://doi.org/10.1029/2006GL025998>, 2006.
- Nicholls, K. W., Abrahamsen, E. P., Heywood, K. J., Stansfield, K., and Østerhus, S.: High-latitude oceanography using the Autosub autonomous underwater vehicle, *Limnology and Oceanography*, 53, 2309–2320, [https://doi.org/10.4319/lo.2008.53.5\\_part\\_2.2309](https://doi.org/10.4319/lo.2008.53.5_part_2.2309), 2008.
- 755 Nicholls, K. W., Østerhus, S., Makinson, K., Gammelsrød, T., and Fahrbach, E.: Ice-ocean processes over the continental shelf of the southern Weddell Sea, Antarctica: A review, *Reviews of Geophysics*, 47, 1–23, 2009.



- Nøst, O. A.: Measurements of ice thickness and seabed topography under the Fimbul Ice Shelf, Dronning Maud Land, Antarctica, *Journal of Geophysical Research: Oceans*, 109, 1–14, 2004.
- 760 Nøst, O. A. and Foldvik, A.: A model of ice shelf-ocean interaction with application to the Filcher-Ronne and Ross Ice Shelves, *Journal of Geophysical Research: Oceans*, 99, 14 243–14 254, <https://doi.org/10.1029/94JC00769>, 1994.
- Nøst, O. A., Biuw, M., Tverberg, V., Lydersen, C., Hattermann, T., Zhou, Q., Smedsrud, L. H., and Kovacs, K. M.: Eddy overturning of the Antarctic Slope Front controls glacial melting in the Eastern Weddell Sea, *Journal of Geophysical Research: Oceans*, 116, 1–17, 2011.
- 765 Núñez-Riboni, I. and Fahrbach, E.: Seasonal variability of the Antarctic Coastal Current and its driving mechanisms in the Weddell Sea, *Deep Sea Research Part I: Oceanographic Research Papers*, 56, 1927–1941, 2009.
- Ohshima, K. I., Takizawa, T., Ushio, S., and Kawamura, T.: Seasonal variations of the Antarctic coastal ocean in the vicinity of Lützw-Holm Bay, *Journal of Geophysical Research: Oceans*, 101, 20 617–20 628, <https://doi.org/10.1029/96JC01752>, 1996.
- Pawlowicz, R.: M\_Map: A mapping package for MATLAB, version 1.4o, [Computer software], URL: [www.eoas.ubc.ca/~rich/map.html](http://www.eoas.ubc.ca/~rich/map.html), 2023.
- 770 Price, M. R., Heywood, K. J., and Nicholls, K. W.: Ice-shelf - ocean interactions at Fimbul Ice Shelf, Antarctica from oxygen isotope ratio measurements, *Ocean Science*, 4, 89–98, <https://doi.org/10.5194/os-4-89-2008>, 2008.
- Prince, H. D. and L'Ecuyer, T. S.: Observed energetic adjustment of the Arctic and Antarctic in a warming world, *Journal of Climate*, <https://doi.org/10.1175/JCLI-D-23-0294.1>, 2024.
- Pritchard, H. D., Ligtenberg, S. R. M., Fricker, H. A., Vaughan, D. G., van den Broeke, M. R., and Padman, L.: Antarctic ice-sheet loss driven  
775 by basal melting of ice shelves, *Nature*, 484, 502–505, 2012.
- Reese, R., Gudmundsson, G. H., Levermann, A., and Winkelmann, R.: The far reach of ice-shelf thinning in Antarctica, *Nature Climate Change*, 8, 53–57, 2018.
- Ribeiro, N., Herraiz-Borreguero, L., Rintoul, S. R., Williams, G., McMahon, C. R., Hindell, M., and Guinet, C.: Oceanic Regime Shift to a Warmer Continental Shelf Adjacent to the Shackleton Ice Shelf, East Antarctica, *Journal of Geophysical Research: Oceans*, 128, e2023JC019 882, <https://doi.org/10.1029/2023JC019882>, 2023.
- 780 Rignot, E., Jacobs, S., Mouginot, J., and Scheuchl, B.: Ice Shelf Melting Around Antarctica, *Science*, 341, 266–270, 2013.
- Rintoul, S. R., Silvano, A., Pena-Molino, B., van Wijk, E., Rosenberg, M., Greenbaum, J. S., and Blankenship, D. D.: Ocean heat drives rapid basal melt of the Totten Ice Shelf, *Science Advances*, 2, e1601 610, <https://doi.org/10.1126/sciadv.1601610>, 2016.
- Ryan, S., Hattermann, T., Darelius, E., and Schröder, M.: Seasonal cycle of hydrography on the eastern shelf of the Filchner Trough, Weddell  
785 Sea, Antarctica, *Journal of Geophysical Research: Oceans*, 122, 6437–6453, 2017.
- Ryan, S., Hellmer, H. H., Janout, M., Darelius, E., Vignes, L., and Schröder, M.: Exceptionally Warm and Prolonged Flow of Warm Deep Water toward the Filchner-Ronne Ice Shelf in 2017, *Geophysical Research Letters*, 47, 1–20, 2020.
- Semper, S. and Darelius, E.: Seasonal resonance of diurnal coastal trapped waves in the southern Weddell Sea, Antarctica, *Ocean Science*, 13, 77–93, 2017.
- 790 Smedsrud, L. H., Jenkins, A., Holland, D. M., and Nøst, O. A.: Modeling ocean processes below Fimbulisen, Antarctica, *Journal of Geophysical Research: Oceans*, 111, 1–13, 2006.
- Steiger, N., Darelius, E., Kimura, S., Patmore, R. D., and Wåhlin, A. K.: The Dynamics of a Barotropic Current Impinging on an Ice Front, *Journal of Physical Oceanography*, 52, 2957 – 2973, <https://doi.org/10.1175/JPO-D-21-0312.1>, 2022.
- Sverdrup, H. U.: The Currents off the Coast of Queen Maud Land, *Norsk Geografisk Tidsskrift*, 14, 239–249, 1954.



- 795 Swithinbank, C., McClain, P., and Little, P.: Drift tracks of Antarctic icebergs, *Polar Record*, 18, 495–501, <https://doi.org/10.1017/S003224740000991>, 1977.
- Thompson, A. F., Stewart, A. L., Spence, P., and Heywood, K. J.: The Antarctic Slope Current in a Changing Climate, *Reviews of Geophysics*, 56, 741–770, 2018.
- Thyng, K. M., Greene, C. A., Hetland, R. D., Zimmerle, H. M., and DiMarco, S. F.: True Colors of Oceanography: Guidelines for Effective and Accurate Colormap Selection, *Oceanography*, 29, 9–13, 2016.
- 800 Tomczak, M.: A multi-parameter extension of temperature/salinity diagram techniques for the analysis of non-isopycnal mixing, *Progress in Oceanography*, 10, 147–171, [https://doi.org/10.1016/0079-6611\(81\)90010-0](https://doi.org/10.1016/0079-6611(81)90010-0), 1981.
- Tomczak, M. and Large, D. G. B.: Optimum multiparameter analysis of mixing in the thermocline of the eastern Indian Ocean, *Journal of Geophysical Research: Oceans*, 94, 16 141–16 149, <https://doi.org/10.1029/JC094iC11p16141>, 1989.
- 805 Turner, J., Guarino, M. V., Arnatt, J., Jena, B., Marshall, G. J., Phillips, T., Bajish, C. C., Clem, K., Wang, Z., Andersson, T., Murphy, E. J., and Cavanagh, R.: Recent Decrease of Summer Sea Ice in the Weddell Sea, Antarctica, *Geophysical Research Letters*, 47, 1–11, 2020.
- Wählin, A. K., Steiger, N., Darelius, E., Assmann, K. M., Glessmer, M. S., Ha, H. K., Herraiz-Borreguero, L., Heuzé, C., Jenkins, A., Kim, T. W., Sommeria, J., and Viboud, S.: Ice front blocking of ocean heat transport to an Antarctic ice shelf, *Nature*, 578, 568–571, 2020.
- Walkden, G. J., Heywood, K. J., Nicholls, K. W., and Abrahamsen, P.: Freshwater transport at Fimbulisen, Antarctica, *Journal of Geophysical Research: Oceans*, 114, <https://doi.org/10.1029/2008JC005028>, 2009.
- 810 Webb, D. J., Holmes, R. M., Spence, P., and England, M. H.: Barotropic Kelvin Wave-Induced Bottom Boundary Layer Warming Along the West Antarctic Peninsula, *Journal of Geophysical Research: Oceans*, 124, 1595–1615, 2019.
- Wählin, A. K., Graham, A. G. C., Hogan, K. A., Queste, B. Y., Boehme, L., Larter, R. D., Pettit, E. C., Wellner, J., and Heywood, K. J.: Pathways and modification of warm water flowing beneath Thwaites Ice Shelf, West Antarctica, *Science Advances*, 7, eabd7254, <https://doi.org/10.1126/sciadv.abd7254>, 2021.
- Zheng, Y., Heywood, K. J., Webber, B. G., Stevens, D. P., Biddle, L. C., Boehme, L., and Loose, B.: Winter seal-based observations reveal glacial meltwater surfacing in the southeastern Amundsen Sea, *Communications Earth & Environment*, 2, 1–9, 2021.
- Zhou, Q., Hattermann, T., Nøst, O. A., Biuw, M., Kovacs, K. M., and Lydersen, C.: Wind-driven spreading of fresh surface water beneath ice shelves in the Eastern Weddell Sea, *Journal of Geophysical Research: Oceans*, 119, 3818–3833, 2014.